

Article

Damage Characteristics and Dynamic Response of RC Shells Subjected to Underwater Shock Wave

Fantong Lin ¹, Xianxiang Zhou ¹, Jian Zhao ¹, Lan Xiao ^{1,*}, Lubo Tang ², Ziyi Liu ¹ and Jianshuai Wang ¹

¹ Defense Engineering Institute, AMS, PLA, Beijing 100850, China; linfantong@126.com (F.L.); zhouxianxiang1@163.com (X.Z.); zhaojian471023@163.com (J.Z.); lzyy0011@163.com (Z.L.); 15200035795@163.com (J.W.)

² School of Civil Engineering, Central South University, Changsha 410083, China; tanglubo@csu.edu.cn

* Correspondence: festoon@sina.com

Abstract: Underwater bottom-sitting shell structures face threats from underwater explosion shock waves. To investigate the damage characteristics and dynamic response of bottom-sitting shell structures under underwater explosion shock waves, three-dimensional numerical models of semi-spherical and semi-cylindrical bottom-sitting reinforced concrete (RC) shells under underwater shock waves were established based on the Arbitrary Lagrangian–Eulerian (ALE) algorithm using LS-DYNA software. The influences of the shock wave transmission medium, explosive equivalent, explosive distance, hydrostatic pressure, and reinforcement on the damage characteristics and dynamic response of semi-spherical and semi-cylindrical bottom-sitting RC shell structures were studied. The results indicated that the damage and center vertical deformation of RC shells under underwater shock waves are significantly greater than those under air shock waves. With an increase in explosive equivalent or decrease in explosive distance, the damage and center vertical deformation of RC shells are increased. The damage to the inner surface of RC shells is more severe than the outer surface. The damage and center vertical deformation of RC shells can be reduced by bottom reinforcement and an increase in the diameter of the steel bar. The ‘hoop effect’ caused by hydrostatic pressure restrains the horizontal convex deformation and slightly decreases the macroscopic damage and vertical center deformation of the semi-spherical RC shell with an increase in hydrostatic pressure within the range of 0–2.0092 MPa. The hydrostatic pressure restrains the horizontal convex deformation of the semi-cylindrical RC shell. However, inward concave deformation of the shell center is increased by hydrostatic pressure, inducing an increase in the damage to and center vertical deformation of the semi-cylindrical RC shell. These findings may offer a reference for the construction and design of protective measures for underwater bottom-sitting shell structures.

Keywords: underwater shock wave; bottom-sitting shell; concrete; damage characteristics; dynamic response



Citation: Lin, F.; Zhou, X.; Zhao, J.; Xiao, L.; Tang, L.; Liu, Z.; Wang, J. Damage Characteristics and Dynamic Response of RC Shells Subjected to Underwater Shock Wave. *Appl. Sci.* **2024**, *14*, 1878. <https://doi.org/10.3390/app14051878>

Academic Editor: Stefano Invernizzi

Received: 18 January 2024

Revised: 19 February 2024

Accepted: 20 February 2024

Published: 25 February 2024



Copyright: © 2024 by the authors. Licensee MDPI, Basel, Switzerland. This article is an open access article distributed under the terms and conditions of the Creative Commons Attribution (CC BY) license (<https://creativecommons.org/licenses/by/4.0/>).

1. Introduction

The development of underwater structures currently faces numerous challenges, such as the threat from underwater explosion shock waves [1,2]. The duration of underwater shock waves is short, but their intensity is extremely high. The excessive stress and strain caused by underwater shock waves affect the integrity of these structures, leading to local failure and potential structural collapse [2]. In recent years, with the increasing number of intentional and unintentional explosions, the impact of explosions on critical infrastructure has received widespread attention [2]. The Nord Stream pipeline, made of 4.1 cm thick steel and encased with 6–11 cm of concrete, placed on the seabed 70–90 m below sea level, was severely damaged by underwater explosion loads. In addition, underwater shock waves present a significant risk to the safety of tunnel structures during the construction or regular use of immersed tube tunnels beneath the seabed. Once an underwater tunnel is

damaged, the whole traffic line may be paralyzed, and these tunnels are difficult to repair within a short time. Therefore, it is essential to evaluate the damage characteristics and dynamic response of underwater structures subjected to underwater explosions.

Currently, several scholars have conducted studies on the dynamic response of shell structures subjected to underwater explosion shock waves. For bottom-sitting shell structures, Yang et al. [2–4] conducted numerical simulation research on the dynamic response of a submerged tube tunnel under underwater shock waves [2], research on the impact of surface shock waves on the dynamic response of the tunnel and its anti-explosion performance [3], and research on the damage assessment of and mitigation measures for submerged tube tunnels under underwater shock waves [4]. Mussa et al. [5] conducted work on the influences of explosive equivalent, lining thickness, and buried depth on the safety of tunnels. The anti-unexpected load design of underwater pipelines is also crucial for the entire service life cycle of offshore oil production and transportation. Wang et al. [6] established a three-dimensional numerical model of the pipeline dynamic response caused by underwater explosion where fluid–solid interaction (FSI) and pipe–seabed interaction (PSI) were considered, and the results indicated that shallow buried laying is an effective way to improve the anti-explosion capability of buried pipelines. However, it should be emphasized that the aforementioned achievements were mostly focused on the response of buried tunnels or pipelines under explosion loads. Corresponding studies of the dynamic behaviors and damage evaluation of underwater unburied bottom-sitting shell structures subjected to explosion loads are very scarce.

Furthermore, there are numerous studies focused on the dynamic response of underwater non-bottom-sitting shell structures, such as underwater suspended tunnels, underwater cylindrical shells, and so on. Kristoffersen et al. [7] assessed the explosion resistance of an underwater floating tunnel with two different section designs subjected to implosion loads, but did not consider the constraint effect and the impact of surrounding water. Luo et al. [8] researched the influence of explosion–vehicle coupled action on the dynamic response of a submerged floating tunnel. Nie et al. [9] researched the impacts of the non-dimensional hull shock factor, reflecting the resilience of the material to shock intensity, slenderness ratio, localized ring stiffener, and endcap on the dynamic buckling modes of underwater cylindrical shells under lateral underwater shock waves. Brochard et al. [10] introduced a simplified damage assessment method for an unstiffened cylindrical shell under underwater initial shock waves and derived the calculation expression of the final deflection of the cylindrical shell. Huang [11] analyzed the transient scattering of spherical pressure pulses by an infinitely long acoustically hard circular cylinder. Jin et al. [12] discussed the dynamic response mode of ship sections under a lateral non-contact water explosion. Hung et al. [13] researched the linear and nonlinear dynamic responses of unstiffened, internally stiffened, and externally stiffened cylindrical shell structures in underwater explosion conditions through water explosion tests and numerical simulation. Peng et al. [14] simulated the damage to and calculated the dynamic response of shell structures under near-field water explosions using SPH and RKPM coupling methods. Nayak et al. [15] predicted the response of coated composite cylindrical shells under near-field water explosions by combining machine learning with high-flux multi-scale finite element (FE) simulation. Long et al. [16] conducted a study on the nonlinear dynamic response of water explosions in double-curved shallow shell of functionally graded material (Sandwich-FGM) sandwich plates based on the first-order shear deformation theory. Numerous studies have been conducted on the dynamic response of underwater non-bottom-sitting shell structures. However, there is a lack of research on the damage to and dynamic response of shells subjected to the coupling of underwater shock waves and hydrostatic pressure. Additionally, there is a scarcity of studies on the effects of reinforcement on the damage and dynamic response of RC shells. Therefore, it is imperative to conduct related research.

Existing research indicates that various materials and shell structure forms are utilized to construct underwater immersed tube tunnels and pipelines. The pressure shell provides a normal working environment for internal equipment and electronic components under-

water, which requires adequate strength and dependable sealing performance [17]. The primary load-bearing structures of immersed tube tunnels and pipelines typically adopt prism or cylindrical shells [18], constructed predominantly from reinforced concrete or steel. The submarine pressure structures commonly adopt a stiffened cylindrical shell composed of a pressure shell and reinforcement [19]. In addition, the pressure spherical shells have been widely used in underwater vehicles and civil engineering fields [20–22]. Therefore, considering the complexity and cost of underwater construction, research on the dynamic response of semi-cylindrical and semi-spherical bottom-sitting RC shell structures subjected to underwater shock waves was conducted.

As the core load of underwater explosions, the underwater shock wave is the research focus. Different from an explosion in air and rock mass, underwater explosion shock waves have high peak overpressure, slow attenuation, and widespread range, and their damage effect on adjacent underwater structures is more severe than on land structures [23,24]. Underwater bottom-sitting shell structures are typically stationary. Besides being vulnerable to precision strikes, they are also susceptible to the effects of non-contact underwater shock waves generated when other targets are struck. Therefore, to further promote the development of the construction and related protection technologies of underwater bottom-sitting shell structures, the influences of the shock wave transmission medium, explosive equivalent, explosive distance, hydrostatic pressure, and reinforcement on the damage characteristics and dynamic response of semi-spherical and semi-cylindrical bottom-sitting RC shell structures subjected to underwater shock waves were studied using validated numerical models.

2. Materials and Validation of the Numerical Simulation

2.1. The Equation of State of the Explosive

When the TNT is detonated, the explosive changes from a concentrated solid to a high-temperature and high-pressure gas. The relationship between the pressure, specific energy, and volume of the explosive product during the energy release process is usually described by the Jones–Wilkins–Lee (JWL) equation:

$$P = A\left(1 - \frac{\omega}{R_1 V}\right)e^{-R_1 V} + B\left(1 - \frac{\omega}{R_2 V}\right)e^{-R_2 V} + \frac{\omega E_0}{V}, \tag{1}$$

where P is the pressure; A , B , ω are pressure coefficients; V is the specific volume; E_0 is the initial specific internal energy; R_1 is the principal eigenvalue; R_2 is a sub-eigenvalue; e is a constant. Explosive parameters are shown in Table 1 [25].

Table 1. The parameters of the JWL equation of state.

A (GPa)	B (GPa)	R_1	R_2	ω	E_0 (GPa)
373.77	3.747	4.15	0.9	0.35	6

2.2. The Equation of State of the Water

The Gruneisen equation of state was used to describe water, where pressure is defined as:

$$p = \begin{cases} \frac{\rho_0 C^2 \mu [1 + (1 - \frac{\gamma_0}{2})\mu - \frac{1}{2}\mu^2]}{1 - (S_1 - 1)\mu - S_2 \frac{\mu^2}{\mu + 1} - S_3 \frac{\mu^3}{(\mu + 1)^2}} + (\gamma_0 + a\mu)E & \mu > 0 \\ \rho_0 C^2 \mu + (\gamma_0 + a\mu)E & \mu < 0 \end{cases}, \tag{2}$$

where the specific volume is $\mu = \rho / \rho_0 - 1$, ρ is the water density, and ρ_0 is the reference density; C is the intercept of particle velocity curve $v_s(v_p)$; S_1 , S_2 , and S_3 are unitless coefficients of the slope of $v_s(v_p)$; γ_0 is dimensionless Gruneisen gamma; a is a unitless first-order volume correction term. The Gruneisen equation of state parameters used in this simulation are shown in Table 2 [26].

Table 2. The parameters of the Gruneisen equation of state.

C (m/s)	S ₁	S ₂	S ₃	a	γ ₀	ρ (kg/m ³)
1647	1.921	−0.096	0	0	0.35	1000

2.3. The Equation of State of the Air

The air adopted the Linear Polynomial equation of state, which is expressed as:

$$P = C_0 + C_1\mu + C_2\mu^2 + C_3\mu^3 + (C_4 + C_5\mu + C_6\mu^2)E_0, \tag{3}$$

where μ is defined as μ = ρ/ρ₀ − 1, where ρ is the air density and ρ₀ is the reference density; the constants C₀–C₆ are the coefficients of EOS; E₀ is initial internal energy per unit reference volume of air. The material parameters of air are shown in Table 3 [27].

Table 3. The parameters of the Linear Polynomial equation of state.

ρ (kg/m ³)	C ₀ –C ₃ , C ₆	C ₄ , C ₅	E ₀	V ₀
1.25	0	0.4	2.53 × 10 ⁵	1.0

2.4. The Material Model of the Concrete

The Riedel–Hiermaier–Thoma (RHT) dynamic damage model proposed by Riedel et al. [28] was adopted for concrete. The curve of pressure p and porosity α during the compression of brittle porous material is shown in Figure 1. Meanwhile, p_{el} is the pressure at which the pores of the material begin to be crushed, and p_{comp} is the pressure when the porous material is fully compacted. In the RHT model, the equation of state for the p–α compaction is:

$$P_R = \frac{1}{\alpha_0} ((B_0 + B_1\mu)\alpha_0\rho_0e + A_1\mu + A_2\mu^2 + A_3\mu^3), \tag{4}$$

where P_R is the pressure for the equation of state; α₀ is the initial porosity; B₀ and B₁ are the polynomial parameters; e is the internal energy per unit mass; μ is the volumetric strain; A₁, A₂, and A₃ are the Hugoniot polynomial coefficients.

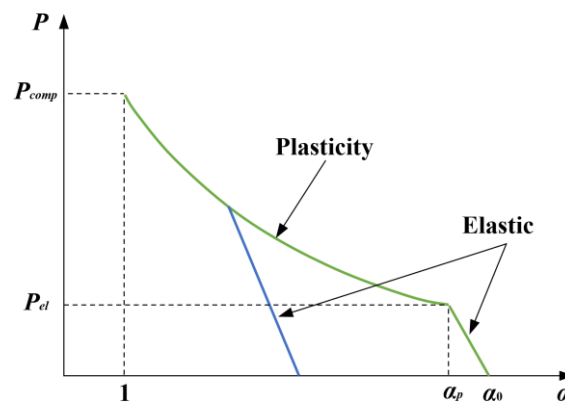


Figure 1. Compression process of brittle porous materials.

The RHT model uses three stress limit surfaces, the initial elastic yield surface, the failure surface, and the residual failure surface, to characterize the behavior of concrete-like materials under high-impact loads, as shown in Figure 2. The RHT model is divided into three phases: the elastic phase, the linear strengthening phase, and the damage softening phase, as shown in Figure 3. The material parameters of RHT are listed in Table 4.

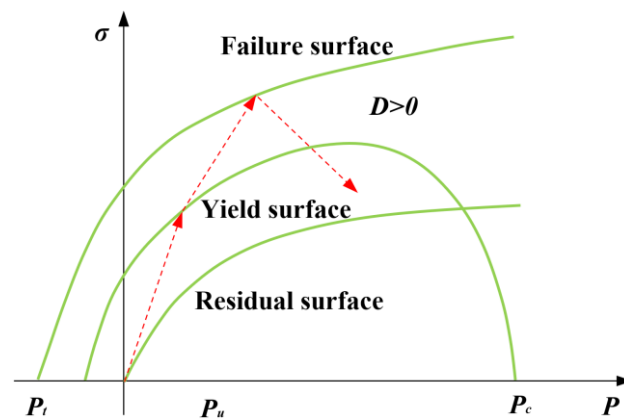


Figure 2. The limit surface of the RHT model.

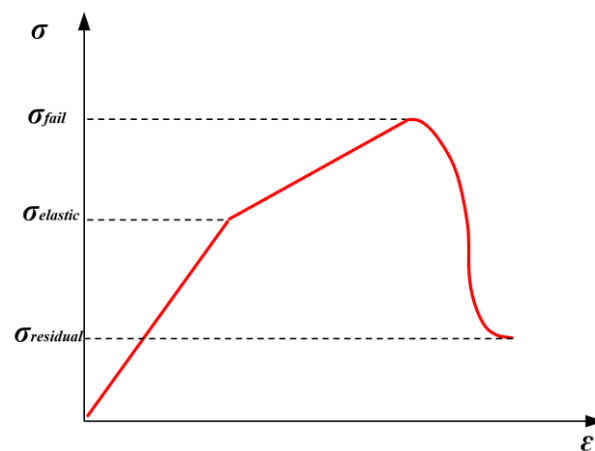


Figure 3. The “three phases” diagram of the RHT constitutive model.

Table 4. The parameters of the RHT model.

Parameter	Value	Parameter	Value
Mass density MID (kg/m ³)	2314	Porosity exponent NP	3.0
Initial porosity ALPHA	1.1884	Reference compressive strain-rate E0C	3.0×10^{-8}
Crush pressure PEL (MPa)	25.33	Reference tensile strain rate E0T	3.0×10^{-9}
Compaction pressure PCO (GPa)	6.0	Break compressive strain rate EC	3.0×10^{22}
Hugoniot polynomial coefficient A1 (GPa)	35.27	Break tensile strain rate ET	3.0×10^{22}
Hugoniot polynomial coefficient A2 (GPa)	39.58	Compressive strain rate dependence exponent BETAC	0.0298507
Hugoniot polynomial coefficient A3 (GPa)	9.04	Tensile strain rate dependence exponent BETAT	0.0344828
Parameter for polynomial EOS B0	1.22	Volumetric plastic strain fraction in tension PTF	0.001
Parameter for polynomial EOS B1	1.22	Compressive yield surface parameter GC*	0.53
Parameter for polynomial EOS T1 (GPa)	35.27	Tensile yield surface parameter GT*	0.7
Parameter for polynomial EOS T2	0	Erosion plastic strain EPSF	2.0
Elastic shear modulus SHEAR (GPa)	16.7	Shear modulus reduction factor XI	0.5
Compressive strength FC (MPa)	38	Damage parameter D1	0.04
Relative tensile strength FT*	0.1	Damage parameter D2	1
Relative shear strength FS*	0.18	Minimum damaged residual strain EPM	0.01
Failure surface Parameter A	1.6	Residual surface parameter AF	1.6
Failure surface Parameter N	0.61	Residual surface parameter NF	0.61
Lode angle dependence factor Q0	0.6805	Gruneisen gamma GAMMA	0
Lode angle dependence factor B	0.0105		

The failure surface Y_{fail} is defined as a function of normalized pressure p^* , Lode Angle θ , and strain rate $\dot{\epsilon}$.

$$Y_{fail} = Y_c(p^*)R_3(\theta)F_{rate}(\dot{\epsilon}), \tag{5}$$

$$Y_c(p^*) = f_c[A(p^* - p_{spall}^*F_{rate}(\dot{\epsilon})^N)], \tag{6}$$

where f_c is the compressive strength; A is the failure surface constant; N is the failure surface index; p^* is the pressure normalized by f_c ; $p_{spall}^* = f_t/f_c$, where f_t is uniaxial tensile strength; $R_3(\theta)$ defines the third invariant of the model as a function of the second and third stress invariants and the meridian ratio Q_2 .

$$R_3(\theta) = \frac{2(1 - Q_2^2)\cos\theta + (2Q_2 - 1)\sqrt{4(1 - Q_2^2)\cos^2\theta - 4Q_2}}{4(1 - Q_2^2)\cos^2\theta + (1 - 2Q_2)^2}, \tag{7}$$

$$\cos(3\theta) = \frac{3\sqrt{3}J_3}{2(J_2)^{3/2}}, \tag{8}$$

$$Q_2 = Q_{2,0} + BQ \cdot p^*, \tag{9}$$

where J_2 and J_3 are the second and third invariants of the deviatoric stress tensor, respectively. $Q_{2,0}$ defines the intensity ratio at zero pressure, and the coefficient BQ defines the rate at which the fracture surface changes from approximately triangular to circular with an increase in pressure.

The strain rate effect is expressed by an increase in the fracture strength with the plastic strain rate. Two different terms can be used for compression and tension, using linear interpolation in the intermediate pressure state.

$$F_{rate}(\dot{\epsilon}) = \begin{cases} 1 + \left(\frac{\dot{\epsilon}}{\dot{\epsilon}_0}\right)^\alpha & \text{for } p > \frac{1}{3}f_c \text{ (compression)} \\ 1 + \left(\frac{\dot{\epsilon}}{\dot{\epsilon}_0}\right)^\delta & \text{for } p < \frac{1}{3}f_c \text{ (tensile)} \end{cases}, \tag{10}$$

where α is the compressive strain rate factor; δ is the tensile strain rate factor; $\dot{\epsilon}_0$ is 3×10^{-6} when stretched and $\dot{\epsilon}_0$ is 3×10^{-5} when compressed.

The elastic limit surface is proportional to the failure surface and can be described as:

$$Y_{elastic} = Y_{fail}F_{cap}(p)F_{elastic}, \tag{11}$$

where $F_{elastic}$ is the ratio of the elastic strength to the failure surface strength along the radial path; $F_{cap}(p)$ is a function limiting the elastic deviator stress under hydrostatic compression, and the pressure between the initial compaction pressure and the solid compaction pressure varies in the range (0, 1).

The residual failure surface can be described as:

$$Y_{residual}^* = Bp^{*M}, \tag{12}$$

where B is the residual failure surface constant; M is the residual failure surface index.

Assuming that damage accumulates due to inelastic partial strain (shear-induced cracking), the relationship is used as:

$$D = \sum \frac{\Delta\epsilon_{pl}}{\epsilon_p^{failure}}, \tag{13}$$

$$\epsilon_p^{failure} = D_1(p^* - p_{spall}^*)^{D_2}, \tag{14}$$

where ε_{pl} is the plastic strain; $\varepsilon_p^{failure}$ is the failure plastic strain; D_1 and D_2 are material constants that describe the effective strain at fracture as a function of pressure.

2.5. The Material Model of the Rebar

The kinematically hardened plastic material model MAT_PLASTIC_KINEMATIC considering the strain rate effect was adopted to model the rebar. Table 5 lists the input parameters of the rebar [29].

Table 5. The parameters of the rebar.

Parameter	Value
Mass density RO (kg/m ³)	7850
Young's modulus E (GPa)	206
Poisson's ratio PR	0.3
Yield stress SIGY (MPa)	400
Strain rate parameter C (s ⁻¹)	35.27
Strain rate parameter P	5
Tangent modulus ETAN (GPa)	2.06

3. Validation of the Numerical Simulation

A field test of RC slab underwater explosion [25] was used to verify the accuracy of numerical methods and material models. The Arbitrary Lagrangian–Eulerian (ALE) method amalgamates the benefits of Lagrangian and Eulerian methods [5] and was used in this model. It should be noted that the material model, solver type, and Euler–Lagrange coupling method are the same as those used in the bottom-sitting shell structures under underwater explosive loads. A numerical analysis model of the 1/2 RC slab under the underwater explosion was established, as shown in Figure 4. The dimensions of the water domain are 0.7 m × 0.7 m × 0.35 m. The dimensions of the RC slab are 0.5 m × 0.5 m × 0.06 m. The fixed boundary is set at the ends of the RC slab. The nodes located on 1/2 symmetrical surface of the model are set to be symmetrical constraints. The outer surface of the water domain is set to be non-reflecting. The RC slab is simulated using the Lagrange algorithm, while the water and TNT are modeled using the Euler algorithm. The interaction between the RC slab and water is simulated through a fluid–structure coupling method. The explosive is set in volume fraction form. The steel bar is simulated using a beam element. The dimensions of the numerical model of the RC slab are shown in Figure 5. Subsequently, based on the experimental data of the dynamic response of the RC slab under underwater explosion [25], the accuracy of the numerical method and material models was verified. As shown in Figure 6, the comparison of the damage characteristics between the underwater explosion test [25] and numerical simulation demonstrates a better consistency. The front side of the plate exhibits minimal damage, characterized by a few distributions of compression cracks. The back side of the plate displays more severe damage, with a large number of tensile cracks dispersed across its surface. Meanwhile, the back side of the plate displays a damage characteristic that the cracks extend from the center to the periphery of the plate.

In addition, as shown in Figure 4, consistent with the underwater explosion test, the pressure measure point 1 and measure point 2 of the underwater explosive are located at the upper and lower surfaces of the plate 130 mm away from the explosive center, respectively [25]. The comparison of the pressure time history curve obtained by the water explosion test [25] and numerical simulation is shown in Figure 7. The overall change trend of the pressure time history curve obtained by numerical simulation is basically consistent with the test data, but there are still some differences. The peak pressure obtained by numerical simulation and underwater explosion test at point 1 is 35.8 Mpa and 40 Mpa, respectively, with a difference of about 10.5%. The peak pressure obtained by numerical simulation and underwater explosion test at measure point 2 is 14.4 Mpa and 16 Mpa, respectively, with a difference of about 10%. The difference between the pressure time

history curve measured by the underwater explosion test and the numerical method may be attributed to the slight movement of the sensor position during the underwater explosion test. In general, the results of the water explosion test and numerical simulation demonstrate better consistency. Therefore, the effectiveness and accuracy of numerical methods and material models of bottom-sitting shell structures under underwater explosive loads have been verified.

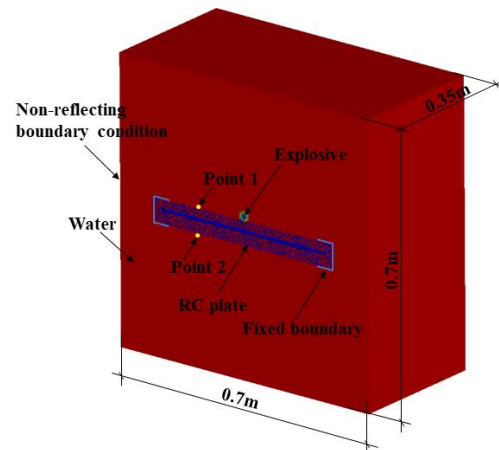


Figure 4. The numerical analysis model of the 1/2 RC slab under underwater explosion.

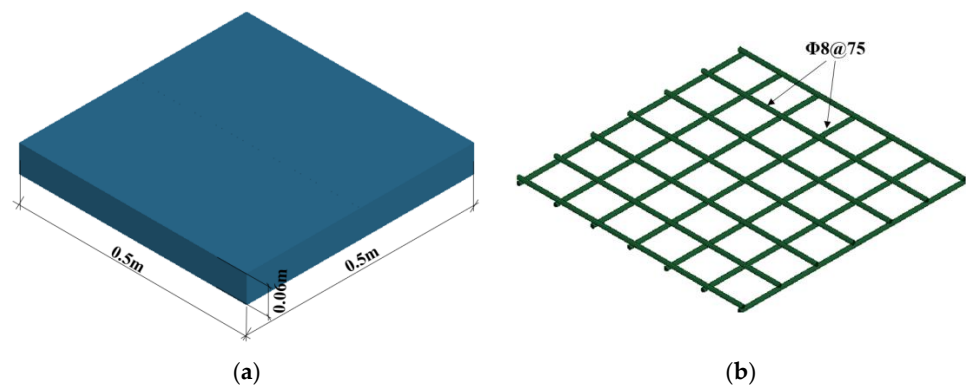


Figure 5. The dimensions of a numerical model of the RC slab: (a) the dimensions of the concrete slab; (b) the diameter and arrangement of the reinforcement [25].

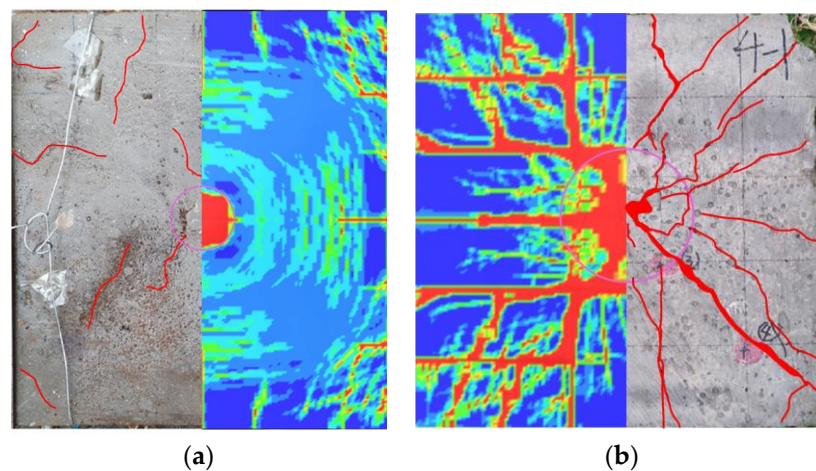


Figure 6. The damage comparison of the underwater RC slab between the underwater explosion test [25] and numerical simulation: (a) the damage distribution on the front; (b) the damage distribution on the back.

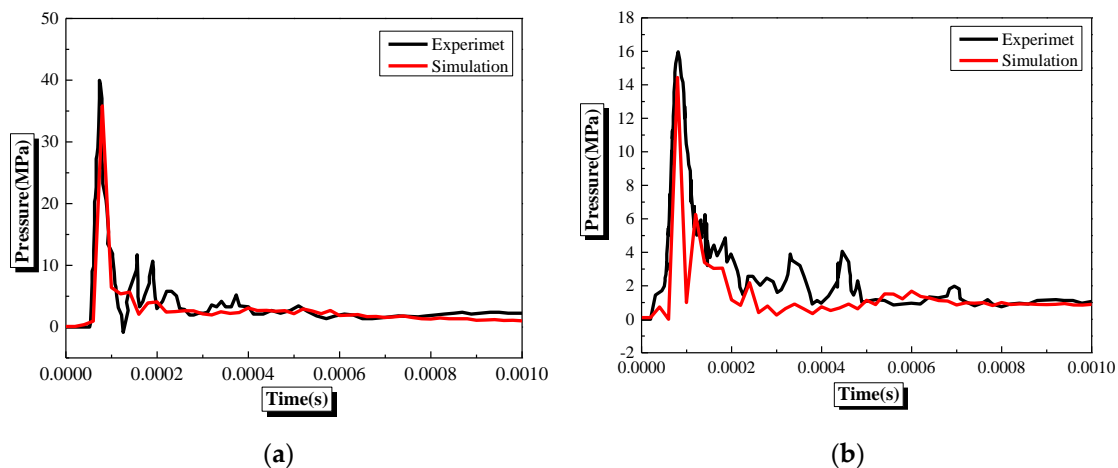


Figure 7. The comparison of the pressure time history curve between the underwater explosion test [25] and numerical simulation: (a) the pressure time history curve at point 1; (b) the pressure time history curve at point 2.

4. Numerical Investigation

4.1. Numerical Model

The schematic diagram of bottom-sitting shell structures subjected to underwater explosive shock waves is shown in Figure 8. The verified numerical method and material models were employed to construct a fully coupled numerical model of an underwater bottom-sitting shell structure with water explosive through LS-DYNA SMP R11.1.0 finite element software, as shown in Figure 9. Due to the symmetry of the structure, the 1/4 symmetry modeling method was used to reduce the mesh number of the model.

The water domain has a 4 m radius at the bottom and a 13 m vertical length of the coupling model of 1/4 semi-spherical RC shell structure with the water explosive. The water domain has a 4 m width at the bottom and a 13 m vertical length of the 1/4 semi-cylindrical RC shell structure–water explosive coupling model. The nodes located on the 1/4 symmetrical surface of the model are set to be symmetrical constraints. The outer surface of the water domain is set to be non-reflecting. The displacements in the x , y , and z directions at the bottom of the semi-spherical and semi-cylindrical RC bottom-sitting shell are set to zero. The shell structure dimensions of semi-spherical and semi-cylindrical RC shells are shown in Figures 10 and 11, respectively. The RC shell is simulated using the Lagrange algorithm, while the air, water, and TNT are modeled using the Euler algorithm. The interaction between the shell and water is simulated using a fluid–structure coupling method, and the explosive is set as volume fraction form. The steel bars are simulated using beam elements. As shown in Figure 9a, the bottom layer of the semi-spherical RC shell structure is reinforced by steel bars with a protective layer thickness of about 45 mm. As shown in Figure 9b, the bottom layer of the semi-cylindrical shell structure is reinforced by steel bars, and the internal and external layers of side walls at both ends are reinforced by steel bars with a protective layer thickness of about 45 mm. In addition, as shown in Figure 12a, the extension of steel bars is concentrated in the top position of the semi-spherical RC shell. As shown in Figure 12b, the extension of steel bars is concentrated in the bottom center position of the side wall of the semi-cylindrical RC shell. To realize the rational distribution of steel bars, the reinforcement mode that gradually reduces steel bars is adopted in the top center of the semi-spherical RC shell and the bottom center of the side wall of the semi-cylindrical RC shell, as shown in Figure 12. The numerical model whose numerical methods and material models have been verified was used to study the effects of the shock wave transmission medium, explosive equivalent, explosive distance, hydrostatic pressure, and reinforcement on the damage characteristics and dynamic response of bottom-sitting RC shell structures under underwater explosive shock waves.

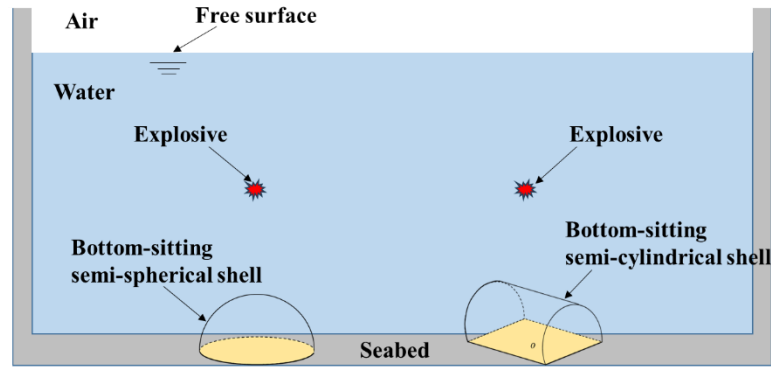


Figure 8. The schematic diagram of bottom-sitting shell structures subjected to underwater explosive shock waves.

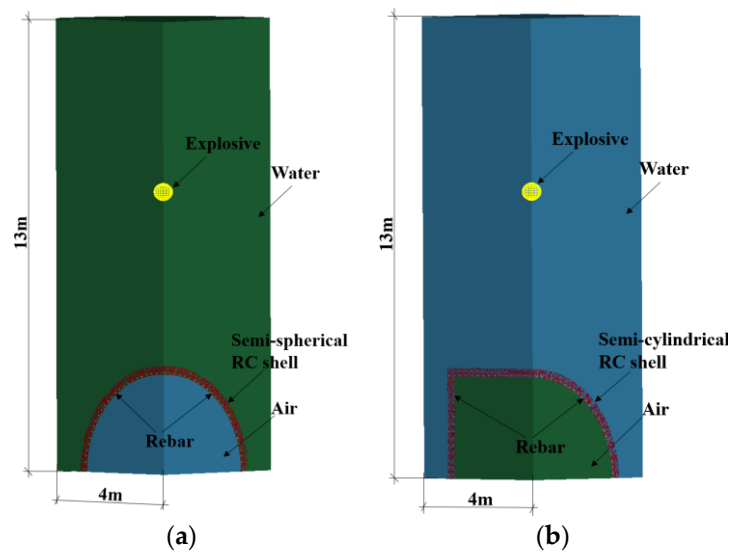


Figure 9. The coupling model of the 1/4 RC shell structure with water and underwater explosive shock waves: (a) the 1/4 semi-spherical RC shell structure with water and underwater explosive shock waves; (b) the 1/4 semi-cylindrical RC shell structure with water and underwater explosive shock waves.

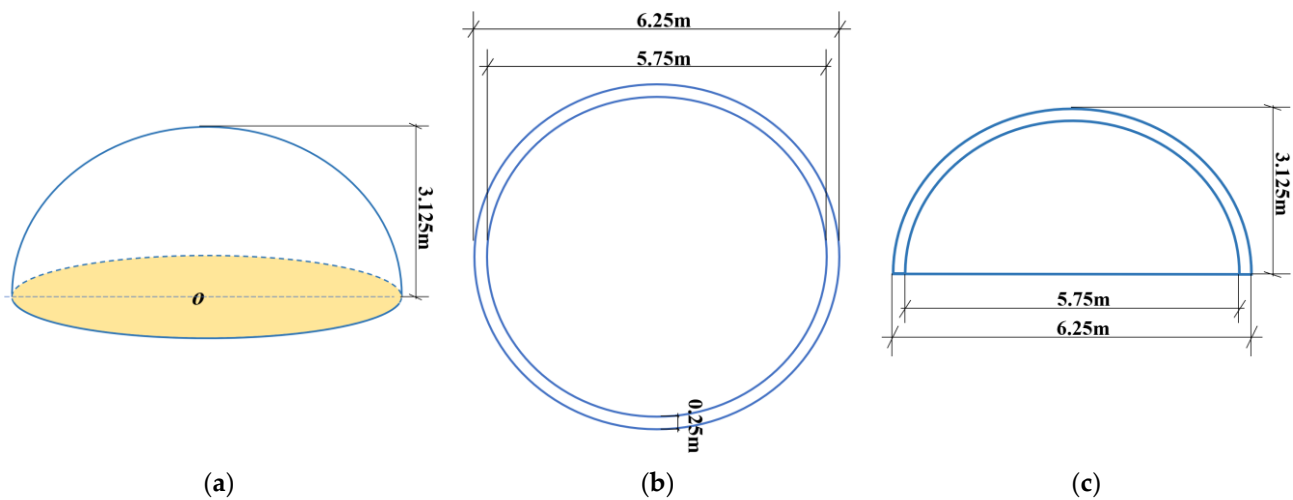


Figure 10. The dimensions of semi-spherical RC shells: (a) the overall structure diagram; (b) the aerial view of the maximum section; (c) the front view of the maximum section.

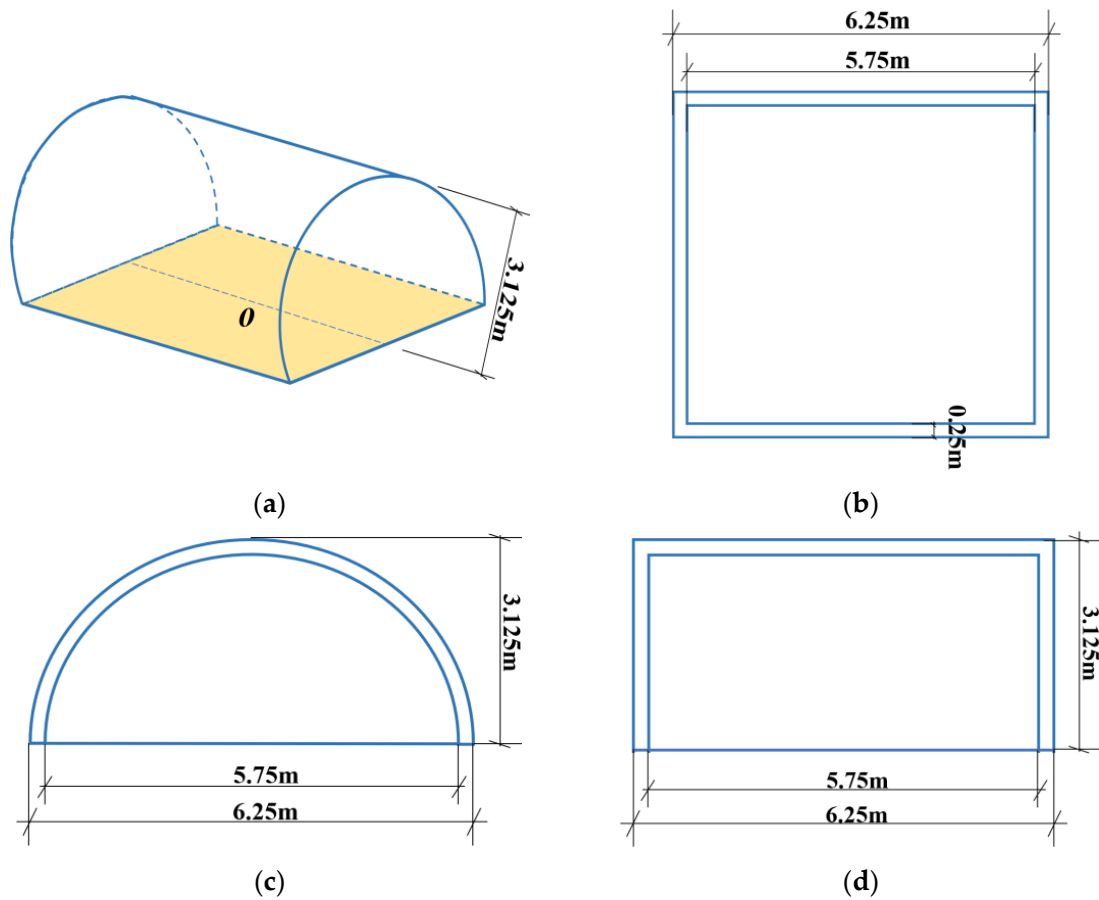


Figure 11. The dimensions of semi-cylindrical RC shells: (a) the overall structure diagram; (b) the aerial view of the maximum section; (c) the side view of the maximum section; (d) the front view of the maximum section.

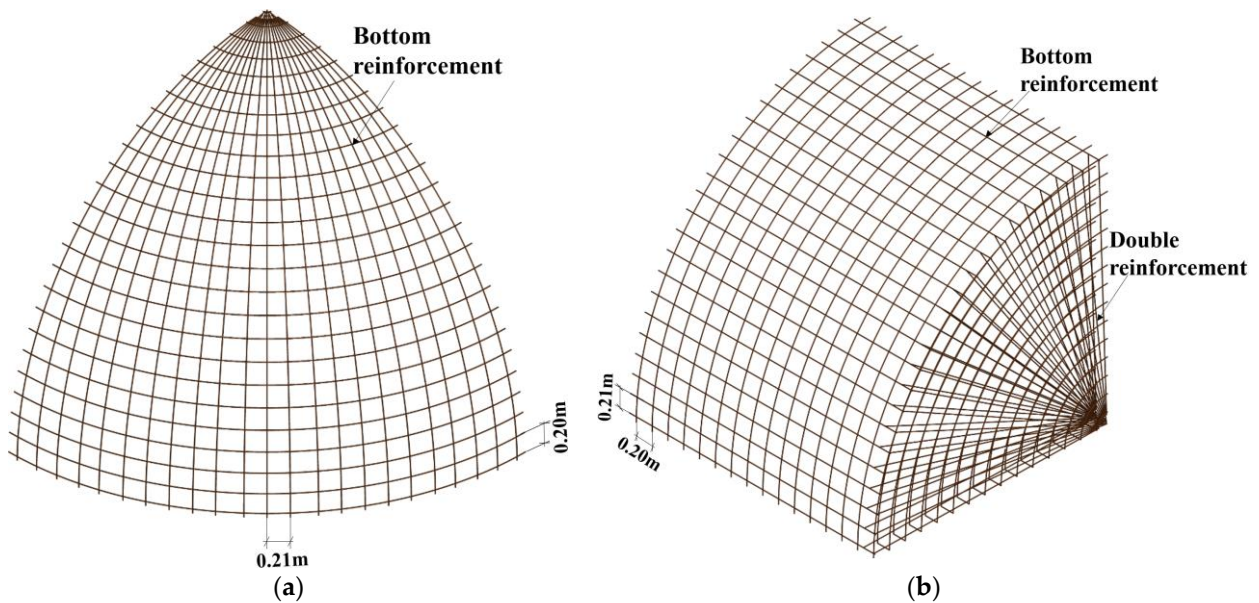


Figure 12. The reinforcement diagram of 1/4 semi-spherical and semi-cylindrical RC shells: (a) the reinforcement of semi-spherical RC shells; (b) the reinforcement of semi-cylindrical RC shells.

4.2. Effects of Shock Wave Transmission Medium on the Damage Characteristics and Dynamic Response of Semi-Spherical and Semi-Cylindrical Bottom-Sitting RC Shells

The attenuation law for shock waves in water is different from that in air, which affects the explosion response of the structure. The density of water is approximately 835 times greater than air. The compressibility of water is 1/30,000–1/2000 that of the air. In addition, shock wave attenuation in water is slow and the capacity of water to store energy is not strong. Therefore, water becomes a good carrier for the propagation of shock waves. The damage caused by water shock waves on surrounding objects surpasses that of air shock waves due to the above factors. The physics of underwater explosions is more complex than that of air explosions, and an equivalent quantity of explosives will cause greater damage to a structure underwater.

Figures 13 and 14 demonstrate the comparative damage distribution on the outer surface of semi-spherical and semi-cylindrical RC shells under 7 m explosive distance and 300 kg explosive equivalent. The annular damage occurs at the bottom of the semi-spherical RC shell near the constraint when subjected to underwater shock waves, whereas there is hardly any damage observed in the semi-spherical RC shell when subjected to air shock waves. The semi-cylindrical RC shell is most prone to damage in the junction of the semi-cylindrical RC shell and side walls at both ends, and the constraint position of the semi-cylindrical RC shell under underwater shock waves. Conversely, the semi-cylindrical RC shell is hardly damaged at all under air shock waves. The structure remains in the elastic deformation stage under air shock waves.

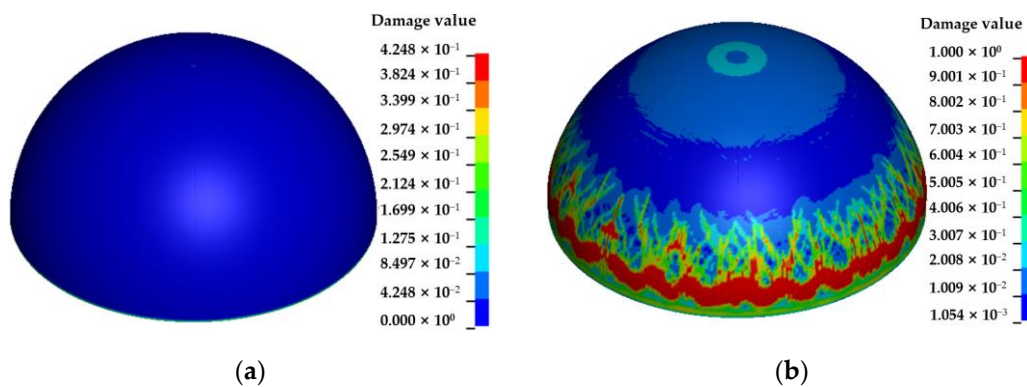


Figure 13. The damage on the outer surface of semi-spherical RC shells under 7 m explosive distance and 300 kg explosive equivalent: (a) the air explosion; (b) the water explosion.

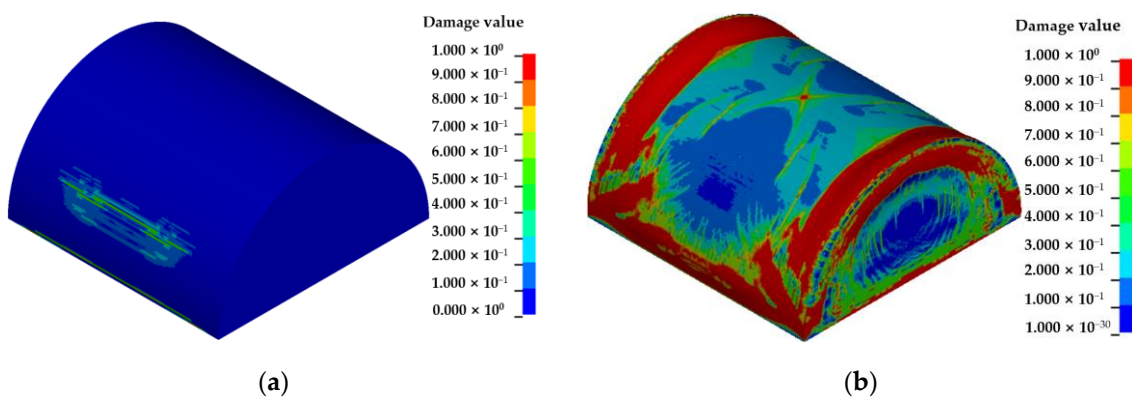


Figure 14. The damage on the outer surface of semi-cylindrical RC shells under 7 m explosive distance and 300 kg explosive equivalent: (a) the air explosion; (b) the water explosion.

Because the resistance of water is greater than air, the attenuation rate of shock waves in water is slow, and the pressure reaching the structure is relatively large, resulting in more significant structural damage. The curves of center vertical displacements of the

semi-spherical and semi-cylindrical RC shell changing with time under 7 m explosive distance and 300 kg explosive equivalent are shown in Figures 15 and 16, respectively. The vertical displacement of the center of the semi-spherical and semi-cylindrical RC shell under underwater shock waves is more significant than under air shock waves. Therefore, the damage and center deformation of semi-spherical and semi-cylindrical RC shells under underwater shock waves are significantly greater than those under air shock waves.

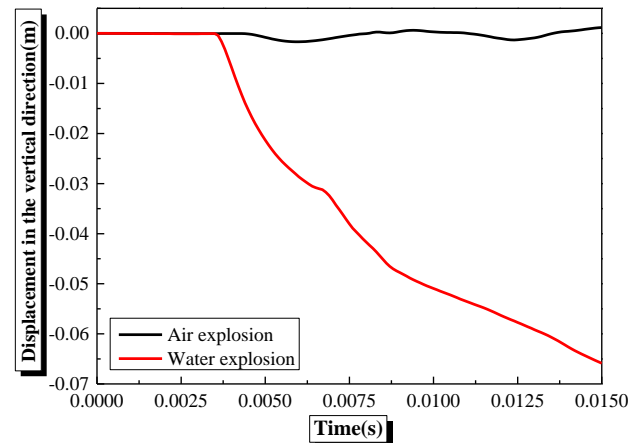


Figure 15. The curves of center vertical displacements of semi-spherical RC shells change with time under 7 m explosive distance and 300 kg explosive equivalent.

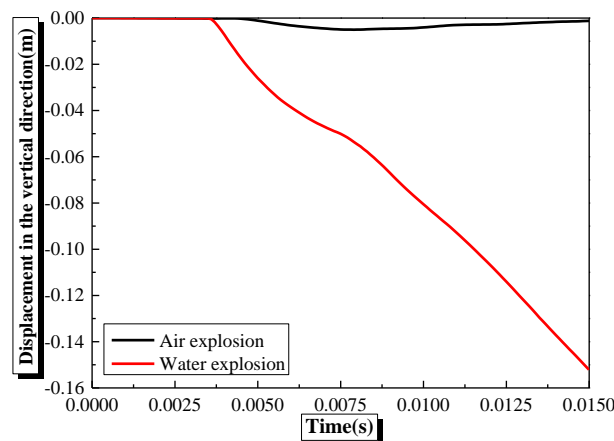


Figure 16. The curves of center vertical displacements of semi-cylindrical RC shells change with time under 7 m explosive distance and 300 kg explosive equivalent.

4.3. Effects of Explosive Equivalent on the Damage Characteristics and Dynamic Response of Semi-Spherical and Semi-Cylindrical Bottom-Sitting RC Shells

The explosive equivalent is an essential factor affecting the dynamic response of structures. Therefore, the explosive equivalent is set as 25 kg, 50 kg, 100 kg, 200 kg, 300 kg, and 500 kg, and the verified numerical model is used to study the damage characteristics and dynamic response of semi-spherical and semi-cylindrical RC shell structures under underwater shock waves at a 5 m explosive distance.

As shown in Figure 17, the overall damage of the semi-spherical RC shell gradually increases with an increase in explosive equivalent at a 5 m explosive distance. The damage is mainly concentrated in the lower part and the center of the semi-spherical RC shell, and gradually extends from the lower part to the center of the semi-spherical RC shell with an increase in explosive equivalent. The semi-spherical RC shell is not damaged when the explosive equivalent is less than or equal to 100 kg at a 5 m explosive distance. The bottom of the semi-spherical RC shell is in a state of complete damage when the explosive

equivalent is greater than or equal to 200 kg at a 5 m explosive distance. In addition, the damage appears in the center, besides the damage at the bottom of the semi-spherical RC shell when the explosive equivalent is greater than or equal to 300 kg at a 5 m explosive distance, and the damage gradually increases with an increase in explosive equivalent. As shown in Figure 18, the damage to the inner surface of the semi-spherical RC shell is more severe than to the outer surface when the explosive equivalent is greater than 200 kg. It is primarily because the outer surface of the semi-spherical RC shell mainly bears the pressure and the concrete has great compressive capacity, but the inner surface of the semi-spherical RC shell mainly bears the tension, and the concrete has poor tensile capacity. In addition, the inner and outer surface of the bottom of the semi-spherical RC shell are significantly damaged due to the large deformation when the explosive equivalent is greater than or equal to 200 kg. As shown in Figure 19, the vertical compression deformation of the semi-spherical RC shell gradually increases with an increase in explosive equivalent. As shown in Figure 20, the vertical displacement of the center of the semi-spherical RC shell increases in a quadratic function form with an increase in explosive equivalent at 0.015 s. The vertical displacement of the center of the semi-spherical RC shell has a maximum value of -0.2462 m when the explosive equivalent is 500 kg. The center displacement of the semi-spherical shell is small and also tends to be stable with time when the explosive equivalent is less than or equal to 100 kg within 0.015 s.

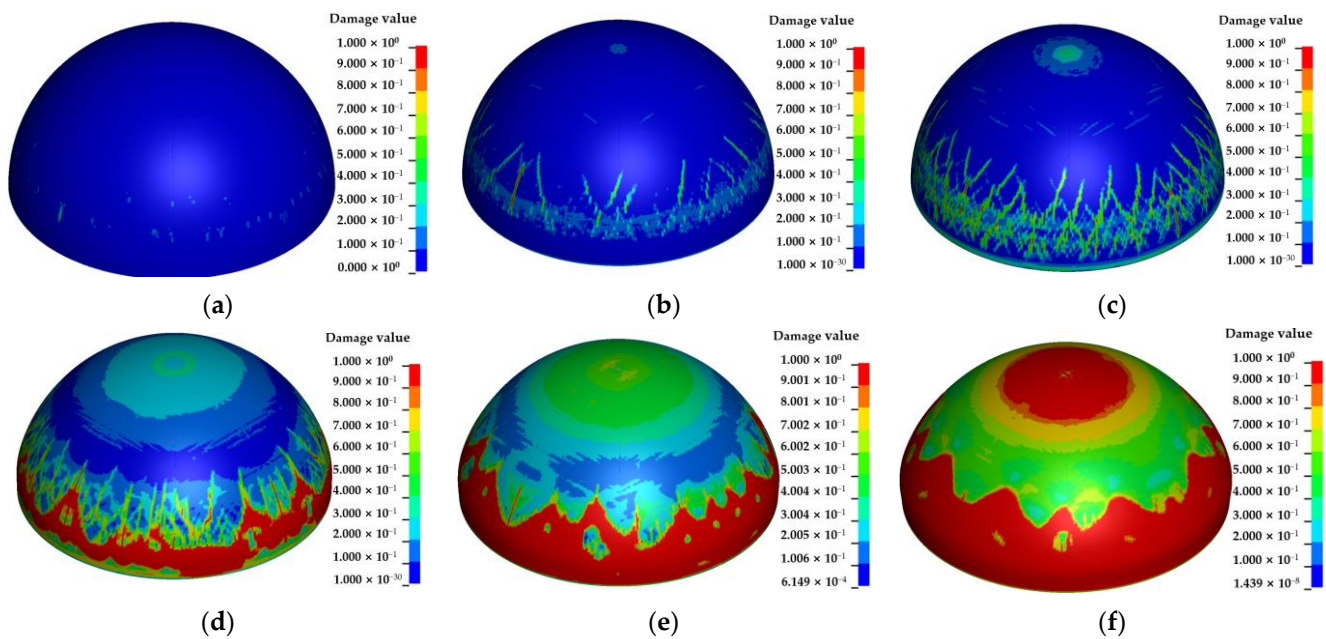


Figure 17. The damage of the outer surface of semi-spherical RC shells at a 5 m explosive distance under different explosive equivalents: (a) 25 kg; (b) 50 kg; (c) 100 kg; (d) 200 kg; (e) 300 kg; (f) 500 kg.

As shown in Figure 21, the overall damage of the semi-cylindrical RC shell gradually increases with an increase in explosive equivalent at a 5 m explosive distance. The damage is mainly concentrated in the junction of the semi-cylindrical RC shell and the side walls at both ends, the constraint position of the semi-cylindrical RC shell, and the center of the semi-cylindrical shell. The damaged area gradually extends from the junction between the semi-cylindrical RC shell and side walls at both ends, and the restraint on both sides of the semi-cylindrical shell to the center of the semi-cylindrical shell with an increase in explosive equivalent.

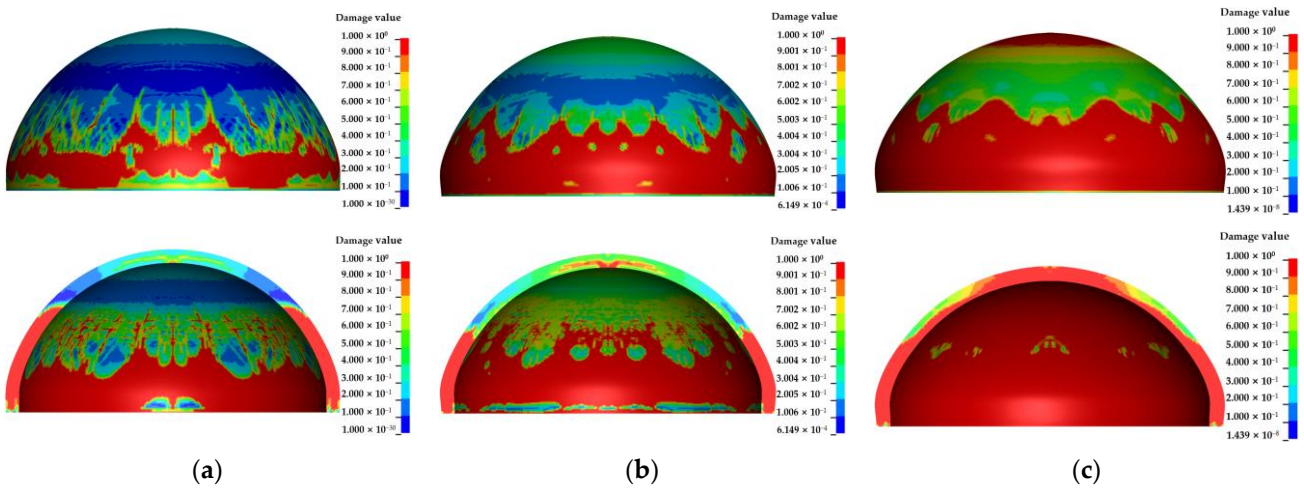


Figure 18. The damage comparison of the outer surface and inner surface of semi-spherical RC shells at a 5 m explosive distance under different explosive equivalents: (a) 200 kg; (b) 300 kg; (c) 500 kg.

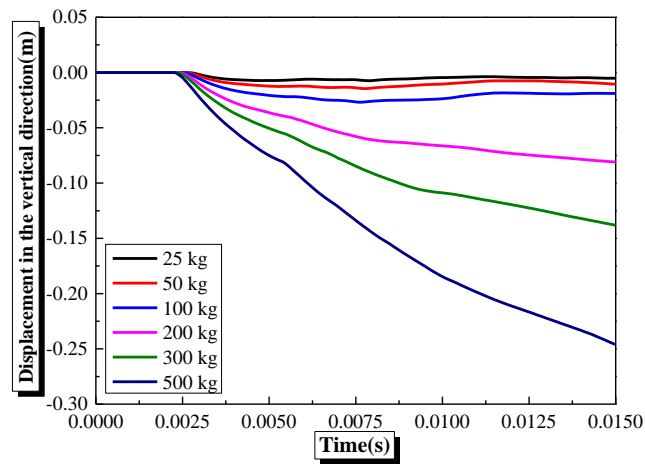


Figure 19. The curves of center vertical displacements of semi-spherical RC shells changing with time at a 5 m explosive distance under different explosive equivalents.

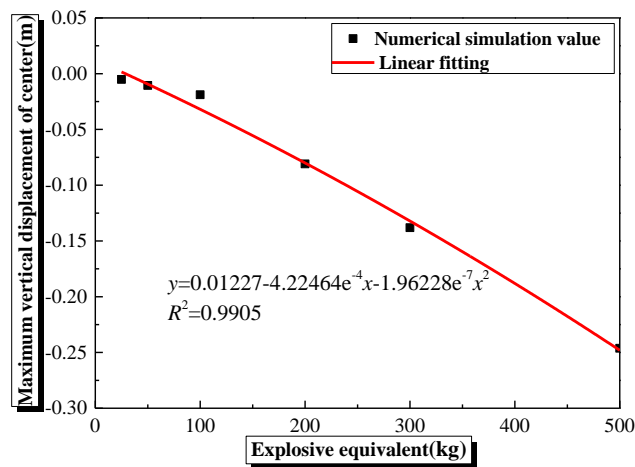


Figure 20. The curves of center maximum vertical displacements of semi-spherical RC shells changing with explosive equivalent at a 5 m explosive distance.

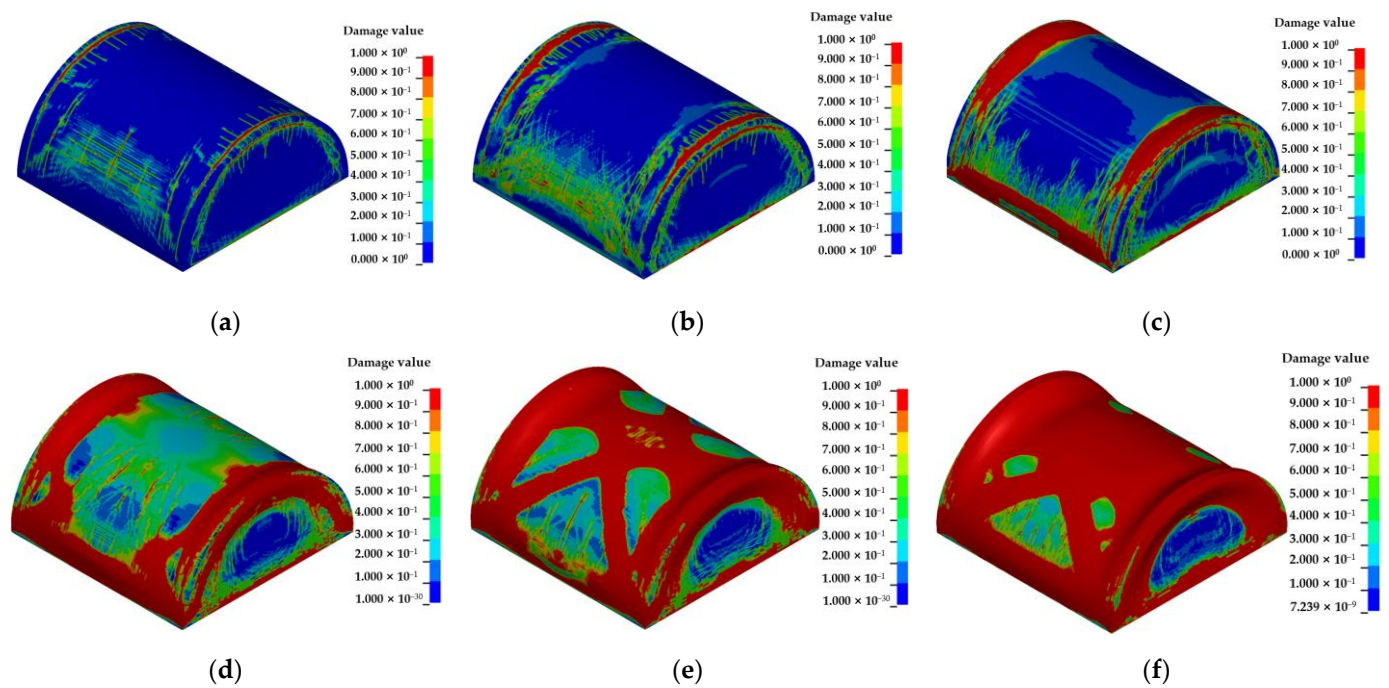


Figure 21. The damage of the outer surface of semi-cylindrical RC shells at a 5 m explosive distance under different explosive equivalents: (a) 25 kg; (b) 50 kg; (c) 100 kg; (d) 200 kg; (e) 300 kg; (f) 500 kg.

The damaged area of the semi-cylindrical RC shell is small when the explosive equivalent is 25 kg and 50 kg, and the damage begins to appear in the junction of the semi-cylindrical RC shell and side walls at both ends, and the bottom restraint of side walls at both ends. The damage begins to appear in the bottom restraint of both sides of the semi-cylindrical shell when the explosive equivalent is 100 kg. The damage starts to appear in the center of the semi-cylindrical shell when the explosive equivalent is 300 kg. Also, the damage in the junction of the semi-cylindrical RC shell and side walls at both ends, and the damage in the bottom restraint of both sides of the semi-cylindrical shell are connected with the damage in the center of the semi-cylindrical shell. The semi-cylindrical shell is damaged, except for the center of side walls at both ends and the part of the two sides of the semi-cylindrical shell when the explosive equivalent is 500 kg. As shown in Figure 22, the damage to the inner surface of the semi-cylindrical RC shell is more severe than the outer surface when the explosive equivalent exceeds 200 kg. It is primarily because the outer surface of the semi-cylindrical RC shell mainly bears the pressure and the concrete has great compressive capacity, whereas the inner surface of the semi-cylindrical RC shell mainly bears the tension and the concrete has low tensile strength. In addition, the inner and outer surfaces in the junction of the semi-cylindrical RC shell and side walls at both ends, the bottom restraint of side walls at both ends, and the bottom restraint of both sides of the semi-cylindrical shell are all seriously damaged due to the large deformation when the explosive equivalent is greater than or equal to 200 kg. As shown in Figure 23, the vertical compression deformation of the RC shell gradually increases with an increase in explosive equivalent. As shown in Figure 24, the vertical displacement of the center of the semi-cylindrical RC shell increases in a quadratic function form with an increase in explosive equivalent at 0.015 s. The vertical displacement of the center of the semi-cylindrical RC shell has a maximum value of 0.36444 m when the explosive equivalent is 500 kg. The center displacement of the semi-cylindrical shell is small when the explosive equivalent is less than or equal to 50 kg within 0.015 s.

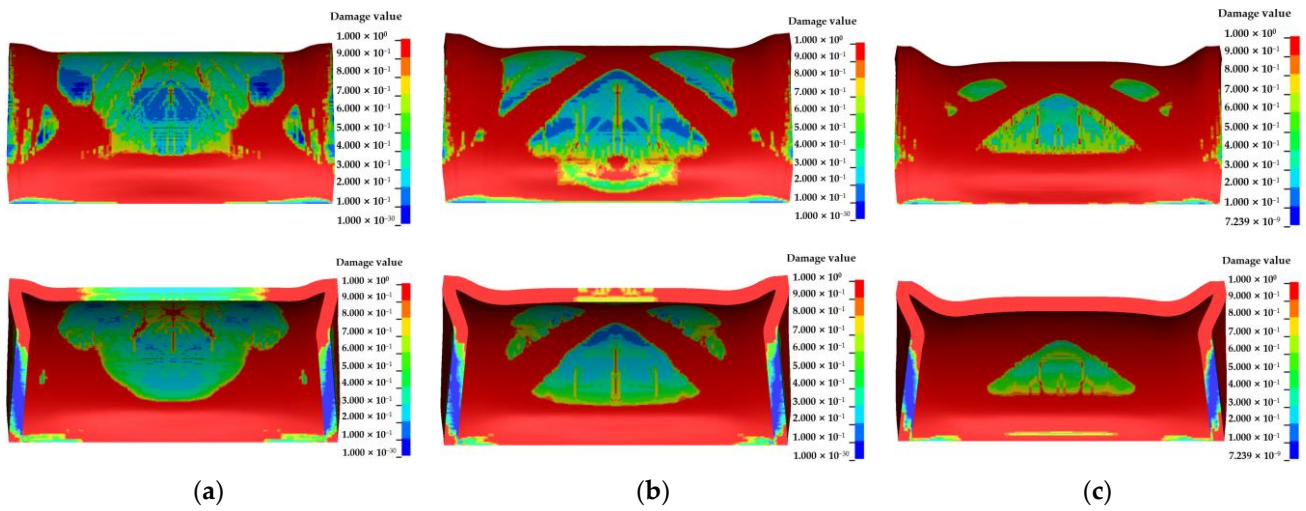


Figure 22. The damage comparison of the outer surface and inner surface of semi-cylindrical RC shells at a 5 m explosive distance under different explosive equivalents: (a) 200 kg; (b) 300 kg; (c) 500 kg.

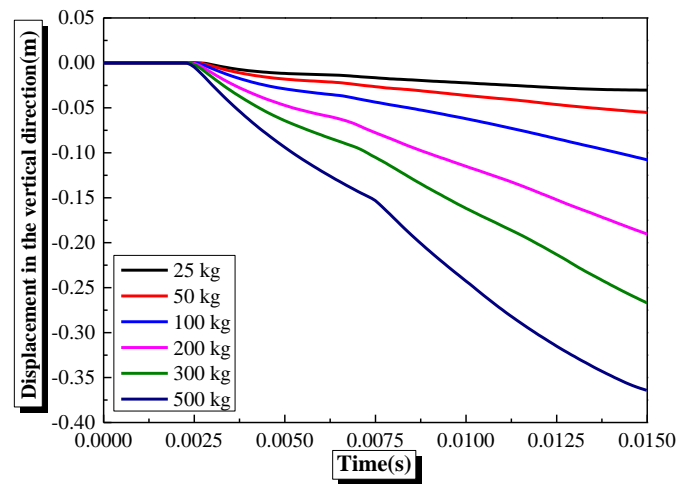


Figure 23. The curves of center vertical displacements of semi-cylindrical RC shells changing with time at a 5 m explosive distance under different explosive equivalents.

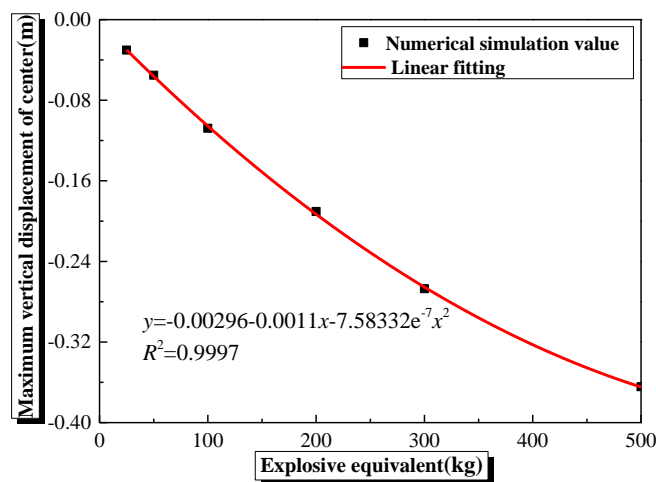


Figure 24. The curves of center maximum vertical displacements of semi-cylindrical RC shells changing with explosive equivalent at a 5 m explosive distance.

4.4. Effects of Explosive Distance on the Damage Characteristics and Dynamic Response of Semi-Spherical and Semi-Cylindrical Bottom-Sitting RC Shells

The explosive distance is an essential factor affecting the structural damage characteristics and dynamic response. Therefore, the explosive distance is set to 3 m, 5 m, 7 m, and 9 m, and the verified numerical model is used to study the damage characteristics and dynamic response of semi-cylindrical and semi-spherical bottom-sitting RC shells under underwater shock waves with a 300 kg explosive equivalent.

As shown in Figure 25, the damage of the semi-spherical RC shell significantly decreases with an increase in the explosive distance. The damage primarily occurs at the center and bottom of the semi-spherical RC shell, and the damaged area has the most significant value when the explosive distance is 3 m. The center of the shell remains undamaged at an explosive distance of 7 m and 9 m. There is minor damage to the semi-spherical RC shell around one-third of its vertical height when the explosive distance is 9 m. As shown in Figure 26, the center displacement of the semi-spherical RC shell decreases significantly with an increase in explosive distance. As shown in Figure 27, the vertical displacement of the center of the semi-spherical RC shell decreases in a power function form with an increase in explosive distance at 0.015 s. The vertical displacement of the center of the semi-spherical RC shell has a minimum value of 0.0302 m when the explosive distance is 9 m. In addition, the vertical displacement of the center of the semi-spherical RC shell at a 3 m explosive distance is larger than at 5 m, 7 m, and 9 m explosive distance.

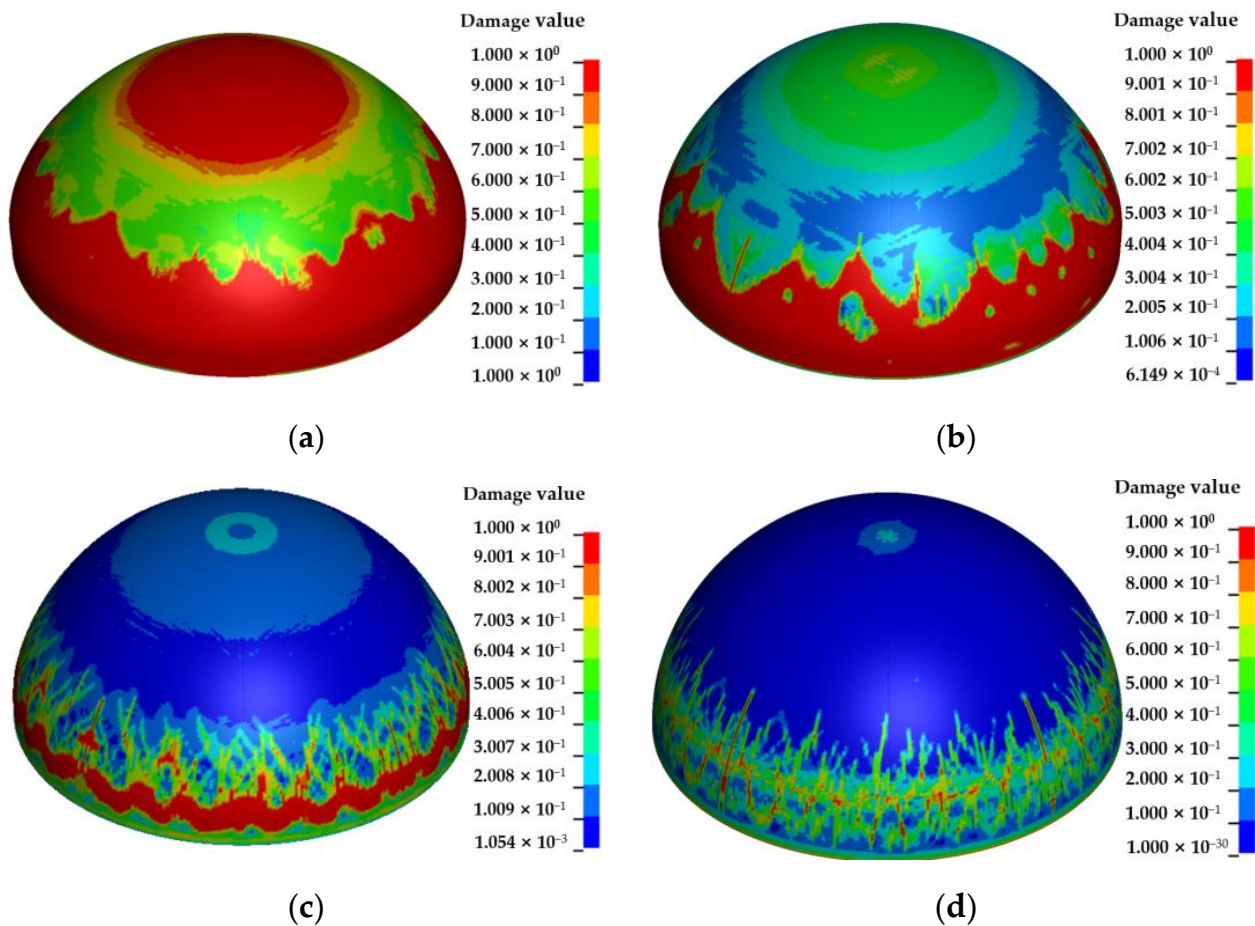


Figure 25. The damage of the outer surface of semi-spherical RC shells with a 300 kg explosive equivalent under different explosive distances: (a) 3 m; (b) 5 m; (c) 7 m; (d) 9 m.

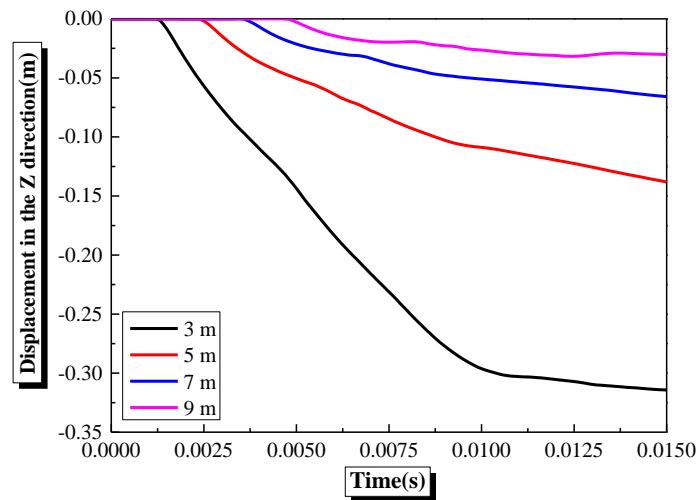


Figure 26. The curves of vertical displacements of the center of semi-spherical RC shells changing with time with a 300 kg explosive equivalent under different explosive distances.

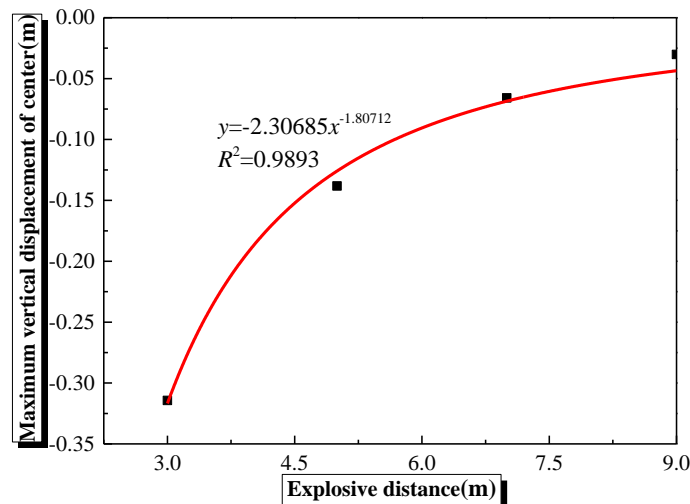


Figure 27. The curves of center maximum vertical displacements of semi-spherical RC shells changing with explosive distance with a 300 kg explosive equivalent.

As shown in Figure 28, the damage of the semi-cylindrical RC shell significantly decreases with an increase in the explosive distance. The damaged area has the most significant value when the explosive distance is 3 m. The damage mainly occurs in the junction of the semi-cylindrical RC shell and side walls at both ends, the constraint position of the semi-cylindrical RC shell, and the center of the semi-cylindrical shell. The center of the semi-cylindrical shell remains undamaged at a 9 m explosive distance. As shown in Figure 29, the center displacement of the semi-cylindrical RC shell significantly decreases with an increase in explosive distance. As shown in Figure 30, the vertical displacement of the center of the semi-cylindrical RC shell decreases in a power function form with an increase in explosive distance at 0.015 s. The vertical displacement of the center of the semi-cylindrical RC shell has a minimum value of 0.0869 m when the explosive distance is 9 m. In addition, the vertical displacement of the center of the semi-cylindrical RC shell at a 3 m explosive distance is larger than at 5 m, 7 m, and 9 m explosive distance.

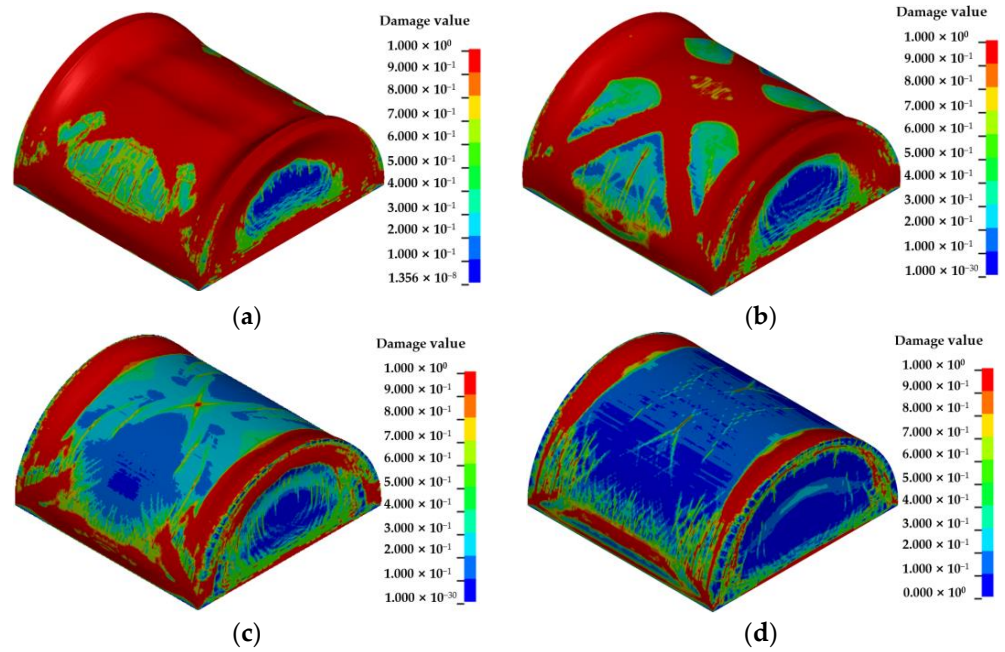


Figure 28. The damage of the outer surface of semi-cylindrical RC shells with a 300 kg explosive equivalent under different explosive distances: (a) 3 m; (b) 5 m; (c) 7 m; (d) 9 m.

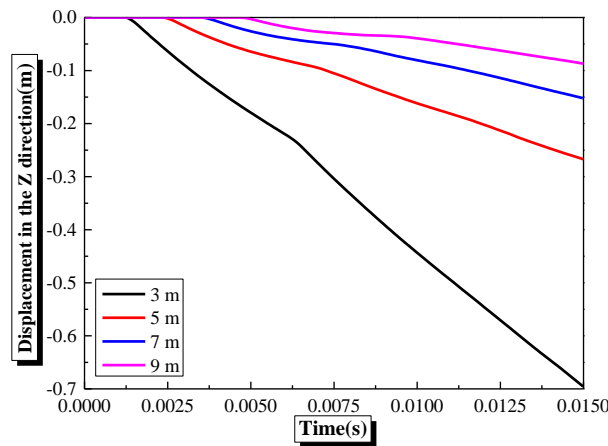


Figure 29. The curves of center vertical displacements of semi-cylindrical RC shells changing with time with a 300 kg explosive equivalent under different explosive distances.

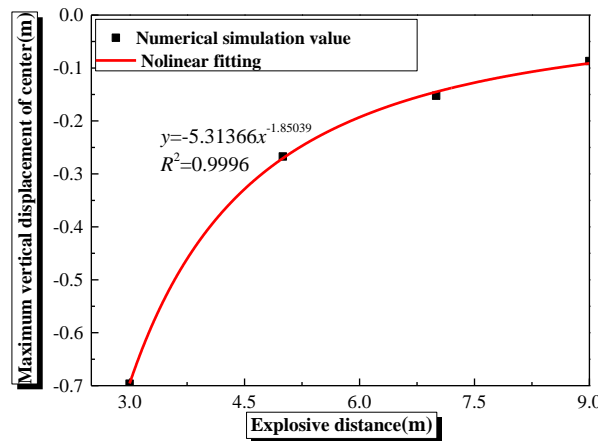


Figure 30. The curves of center maximum vertical displacements of semi-cylindrical RC shells changing with explosive distance with a 300 kg explosive equivalent.

4.5. Effects of Bottom Reinforcement on the Damage Characteristics and Dynamic Response of Semi-Spherical and Semi-Cylindrical Bottom-Sitting RC Shells

The tensile properties of ordinary concrete materials are inadequate, and the reinforcement located in the main tensile area of the concrete significantly affects the damage characteristics and dynamic response of semi-spherical and semi-cylindrical bottom-sitting RC shells. Therefore, the damage characteristics and dynamic response of semi-spherical and semi-cylindrical shells with different reinforcement are studied under 200 kg explosive equivalent and 5 m explosive distance.

As shown in Figure 31, the surface damage area of unreinforced semi-spherical concrete shells is significantly larger than RC shells. Additionally, the surface damage area of the semi-spherical RC shell with 10 mm steel reinforcement is significantly larger than with 16 mm steel reinforcement when the explosive equivalent is 200 kg and the explosive distance is 5 m. The semi-spherical concrete shell exhibits large damage cracks extending upwards from the bottom damage area compared with the RC shell. It suggests that the reinforced semi-spherical shell has better ductility and bottom reinforcement can narrow the large cracks of the semi-spherical RC shell into smaller cracks. As shown in Figure 32, the central displacement of the unreinforced semi-spherical shell is significantly greater than that of the reinforced semi-spherical shell, and the central displacement of the semi-spherical RC shell decreases significantly with an increase in the diameter of the steel bar. Therefore, the overall damage and center vertical deformation of the semi-spherical shell can be reduced by bottom reinforcement and an increase in the diameter of the steel bar within the diameter range of 10–16 mm.

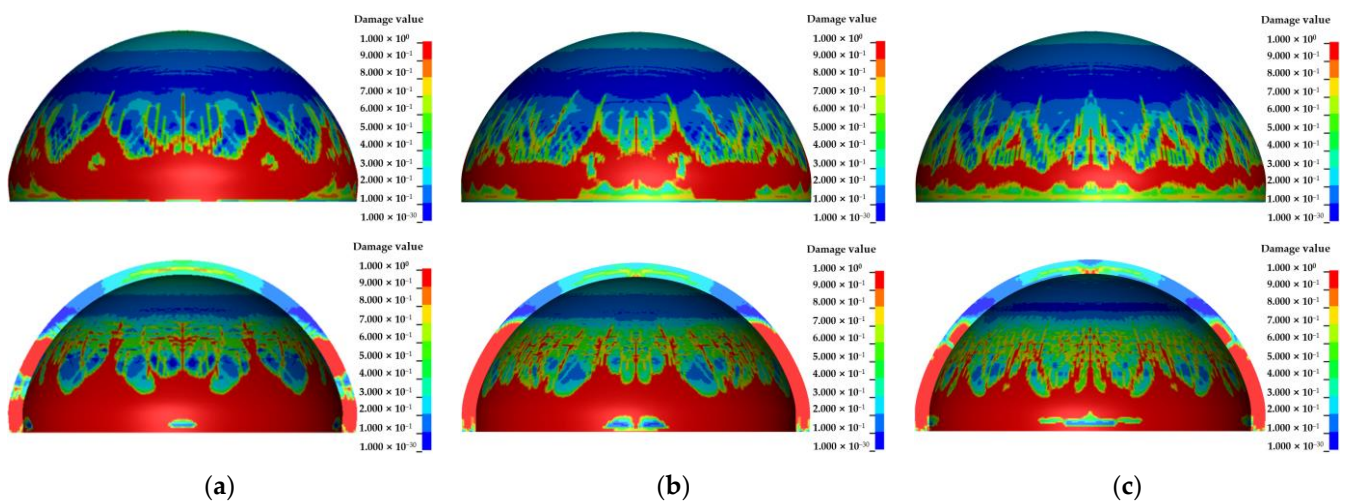


Figure 31. The surface damage of semi-spherical RC shells under different reinforcement diameters with 200 kg explosive equivalent and 5 m explosive distance: (a) unreinforced; (b) reinforced—10 mm; (c) reinforced—16 mm.

As shown in Figure 33, the surface damage area of unreinforced semi-cylindrical shells is significantly larger than that of RC semi-cylindrical shells. Additionally, the surface damage area of the semi-cylindrical RC shell with 10 mm steel reinforcement is significantly larger than with 16 mm steel reinforcement. The damage in the center of the unreinforced semi-cylindrical shell is greater than that of the reinforced semi-cylindrical shell. The outer surface of the reinforced semi-cylindrical RC shell has hardly any damage in the central area, and the inner surface has a small amount of damage. As shown in Figure 34, the central displacement of the unstiffened semi-cylindrical shell is more significant than the reinforced semi-cylindrical shell, and the central displacement of the semi-cylindrical RC shell slightly decreases with an increase in the diameter of the steel bar. Therefore, the overall damage and vertical deformation of the semi-cylindrical shell can be reduced by bottom reinforcement and an increase in the diameter of the steel bar within the diameter

range of 10–16 mm, but the diameter of the steel bar has little effect on the vertical center deformation of the semi-cylindrical RC shell.

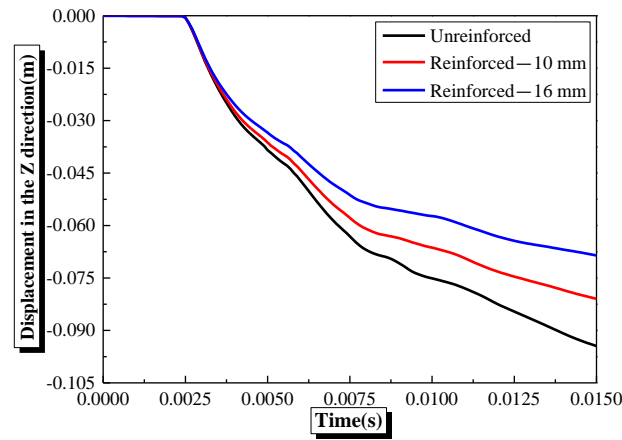


Figure 32. The curves of center vertical displacements of semi-spherical RC shells changing with time with 200 kg explosive equivalent and 5 m explosive distance under different reinforcement diameters.

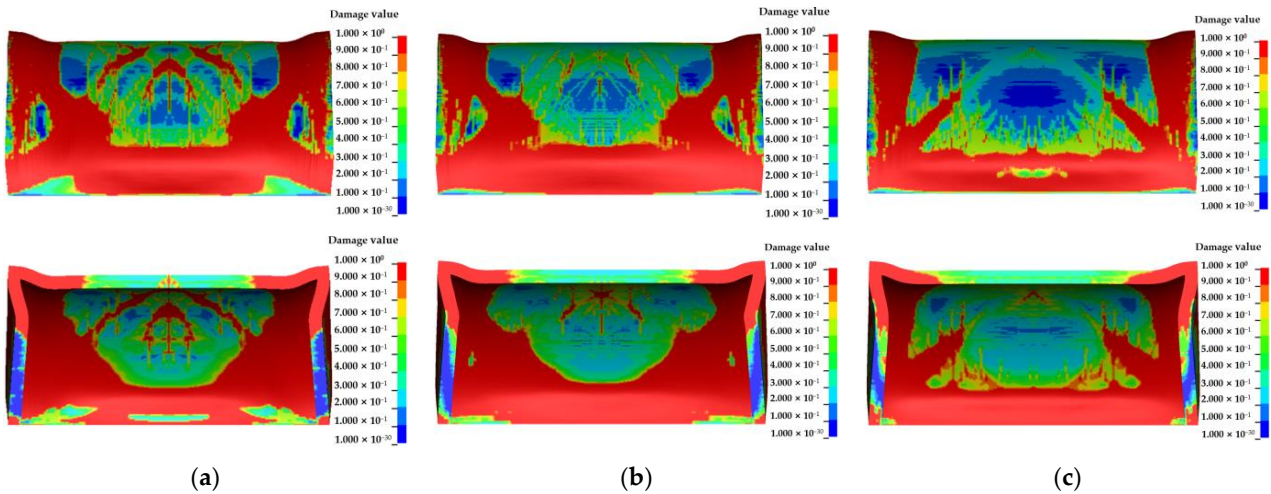


Figure 33. The damage of the surface of semi-cylindrical RC shells under different reinforcement diameters with 200 kg explosive equivalent and 5 m explosive distance: (a) unreinforced; (b) reinforced—10 mm; (c) reinforced—16 mm.

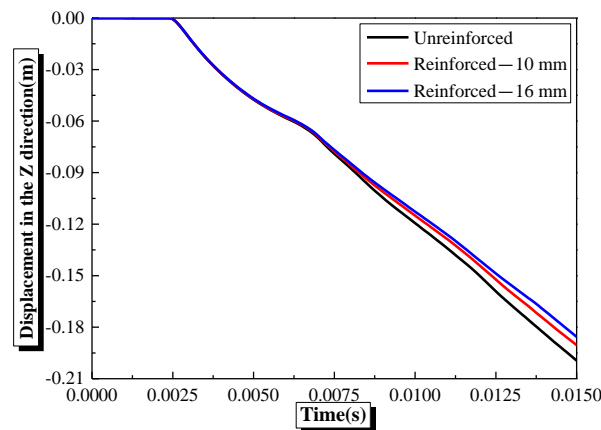


Figure 34. The curves of center vertical displacements of semi-cylindrical RC shells changing with time with 200 kg explosive equivalent and 5 m explosive distance under different reinforcement diameters.

4.6. Effects of Hydrostatic Pressure on the Damage Characteristics and Dynamic Response of Semi-Spherical and Semi-Cylindrical Bottom-Sitting RC Shells

The coupling of hydrostatic pressure and underwater shock waves may lead to structural damage to underwater structures. Therefore, the initial hydrostatic pressure is set as 0 MPa, 0.50225 MPa, 1.0045 MPa, and 2.009 MPa, to study the damage characteristics and dynamic response of semi-spherical and semi-cylindrical bottom-sitting RC shells with 7 m explosive distance and 300 kg explosive equivalent.

As shown in Figure 35, the damage is mainly concentrated in the lower part of the shell, and relatively severe annular damage occurs near the bottom of the shell. As shown in Figure 36, the damaged area and center displacement of the semi-spherical RC shell slightly decrease with an increase in hydrostatic pressure within the hydrostatic pressure range of 0–2.0092 MPa. The schematic diagram of the deformation in semi-spherical RC shell cross-section is shown in Figure 37. The curves of horizontal displacements of the semi-spherical RC shell changing with α with 300 kg explosive equivalent and 7 m explosive distance under different hydrostatic pressures are shown in Figure 38. The maximum horizontal displacement is located in the damaged area of the semi-spherical shell. The maximum horizontal displacement of the semi-spherical shell under a hydrostatic pressure of 0 MPa is more significant than under a hydrostatic pressure of 2.0092 MPa. The hydrostatic pressure on the surface of the semi-spherical RC shell causes a ‘hoop effect’ that restrains the horizontal convex deformation of the semi-spherical RC shell and reduces the damage area at the bottom of the semi-spherical RC shell. Additionally, with an increase in hydrostatic pressure, the horizontal convex deformation of the semi-spherical RC shell decreases, improving the vertical bearing capacity and reducing the vertical center displacement of semi-spherical RC shells within the hydrostatic pressure range of 0–2.0092 MPa.

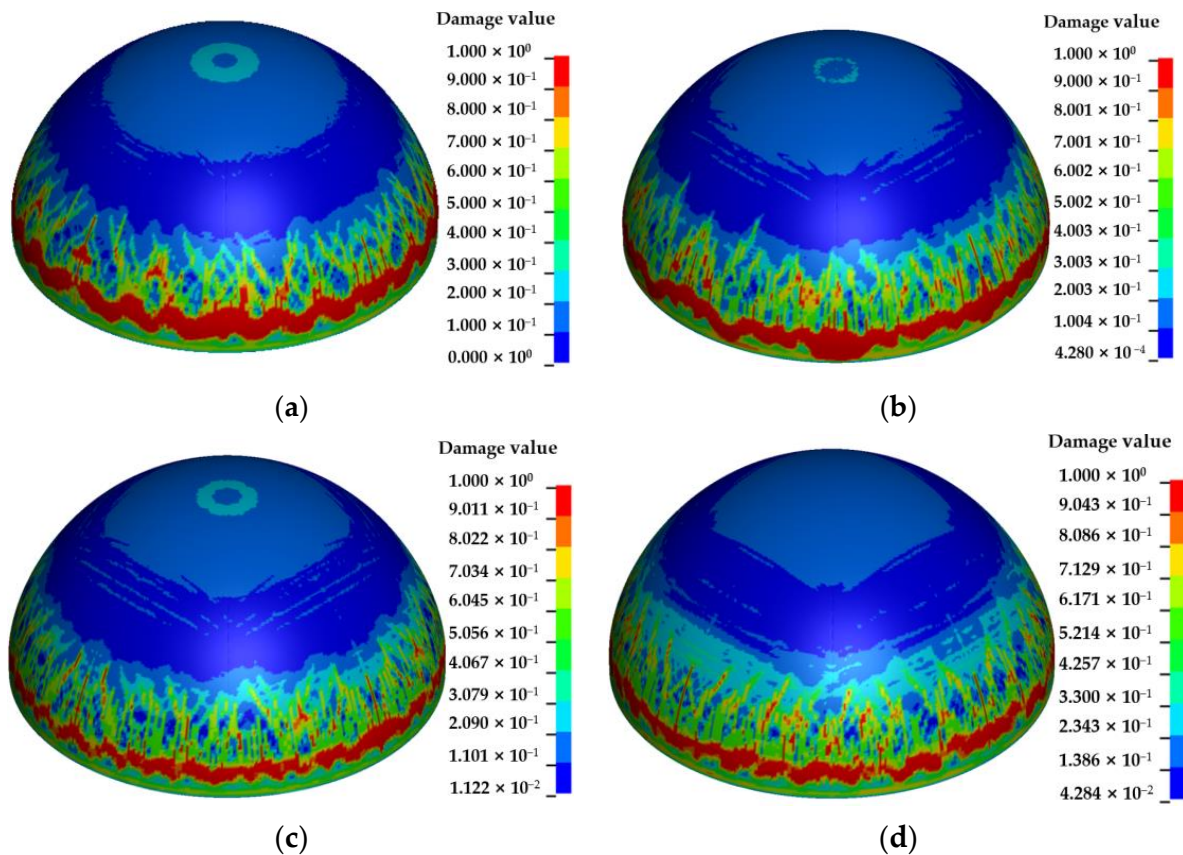


Figure 35. The damage of the surface of semi-spherical RC shells under different hydrostatic pressures with 300 kg explosive equivalent and 7 m explosive distance: (a) 0 MPa; (b) 0.5023 MPa; (c) 1.0046 MPa; (d) 2.0092 MPa.

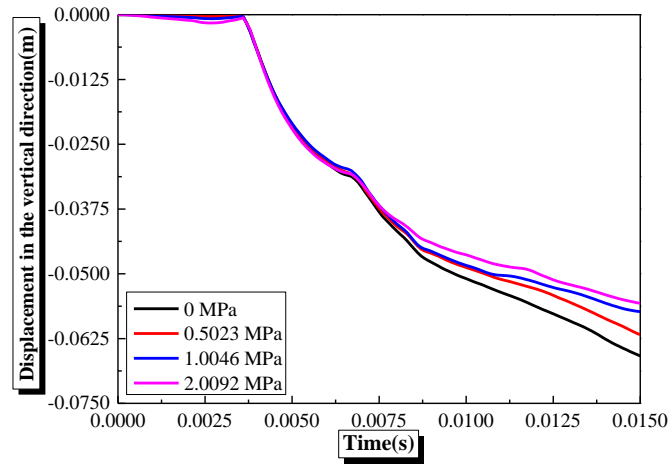


Figure 36. The curves of center vertical displacements of semi-spherical RC shells changing with time with 300 kg explosive equivalent and 7 m explosive distance under different hydrostatic pressures.

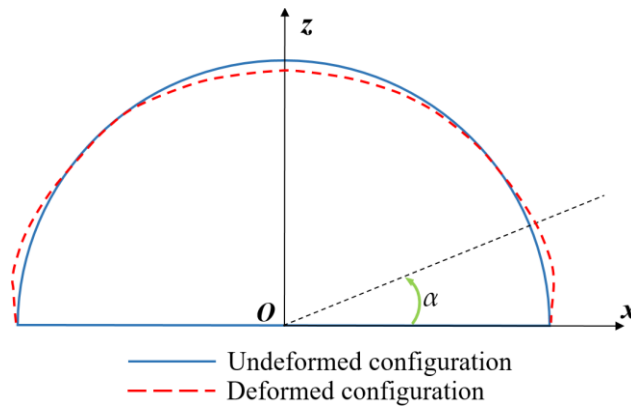


Figure 37. The schematic diagram of the deformation in the semi-spherical RC shell cross-section.

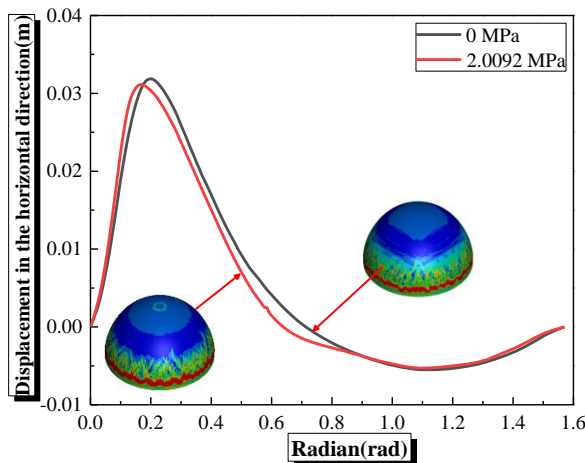


Figure 38. The curves of horizontal displacements of semi-spherical RC shells changing with α with 300 kg explosive equivalent and 7 m explosive distance under different hydrostatic pressures.

As shown in Figure 39, the damage of the semi-cylindrical RC shell gradually increases with an increase in hydrostatic pressure within the range of 0–2.0092 MPa. The increased damage is mainly concentrated in the middle area of the shell. As shown in Figure 40, the hydrostatic pressure increases the central displacement of the semi-cylindrical RC shell. However, the variation amplitude is relatively small. The schematic diagram of the

deformation in the semi-cylindrical RC shell cross-section is shown in Figure 41. The curves of horizontal displacements of the semi-cylindrical RC shell changing with β with 300 kg explosive equivalent and 7 m explosive distance under different hydrostatic pressures are shown in Figure 42. The maximum horizontal displacement is located in the damaged area of the semi-cylindrical RC shell. The maximum horizontal displacement of the semi-cylindrical RC shell under hydrostatic pressure of 0 MPa is more significant than under hydrostatic pressure of 2.0092 MPa. The horizontal convex deformation of the semi-cylindrical RC shell is constrained by the hydrostatic pressure. However, the vertical bearing capacity of the center of the semi-cylindrical RC shell is weaker than that of the semi-spherical RC shell. Therefore, the coupling of hydrostatic pressure and underwater shock waves increases the inward concave deformation of the shell center, inducing an increase in the vertical displacement and center damage of the semi-cylindrical RC shell.

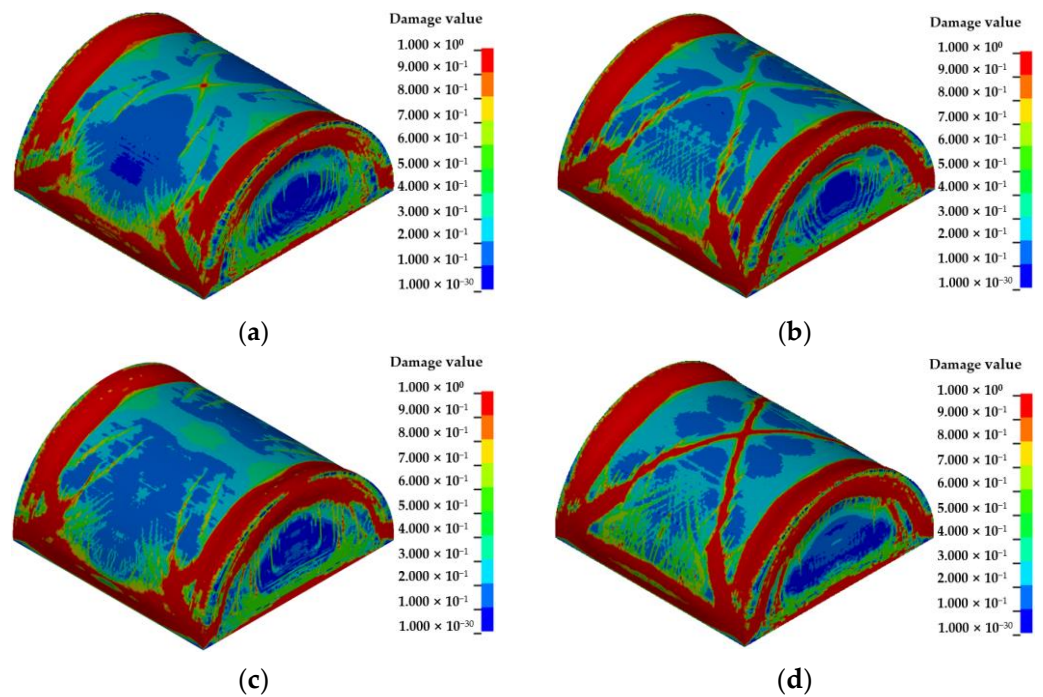


Figure 39. The damage of the surface of semi-cylindrical RC shells under different hydrostatic pressures with 300 kg explosive equivalent and 7 m explosive distance: (a) 0 MPa; (b) 0.5023 MPa; (c) 1.0046 MPa; (d) 2.0092 MPa.

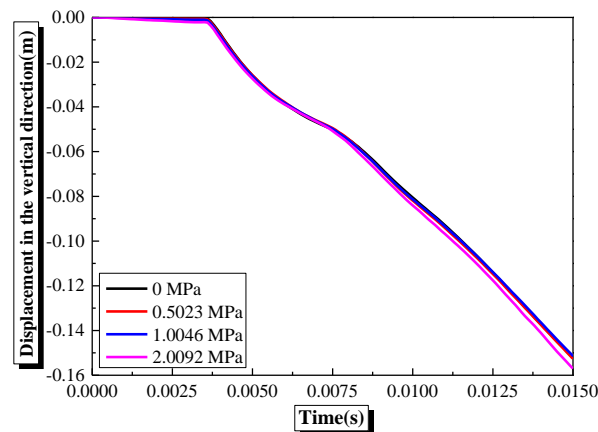


Figure 40. The curves of center vertical displacements of semi-cylindrical RC shells changing with time with 300 kg explosive equivalent and 7 m explosive distance under different hydrostatic pressures.

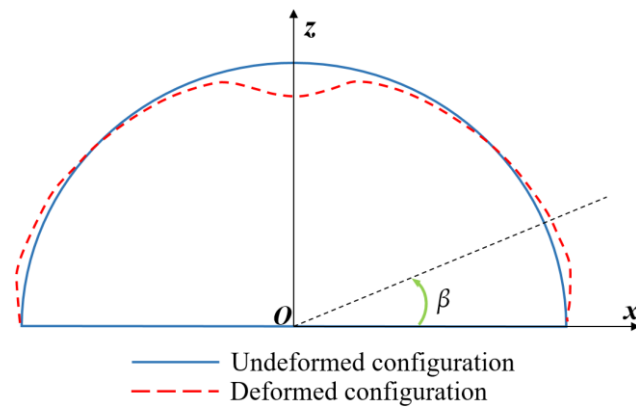


Figure 41. The schematic diagram of the deformation in the semi-cylindrical RC shell cross-section.

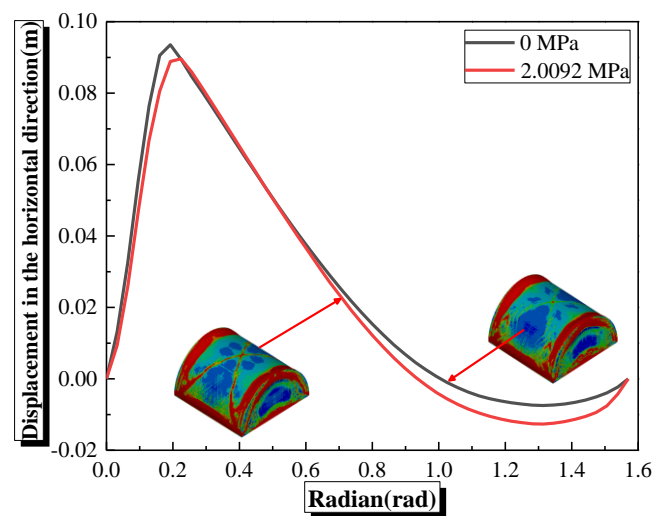


Figure 42. The curves of horizontal displacements of semi-cylindrical RC shells changing with β with 300 kg explosive equivalent and 7 m explosive distance under different hydrostatic pressures.

5. Discussion

The damage characteristics and dynamic response of semi-spherical and semi-cylindrical bottom-sitting RC shells subjected to underwater shock waves were studied based on the Arbitrary Lagrangian–Eulerian (ALE) algorithm using LS-DYNA software. The water increases the damaging effect of an explosion compared to air. With an increase in explosive equivalent or decrease in explosive distance, RC shells are damaged more severely. Steel bars increase the anti-explosion capacity of RC shells. The water around the RC shells forms a ‘hoop effect’ within a certain range of hydrostatic pressure, which decreases the horizontal convex deformation of RC shells under explosion shock waves. However, the inward concave deformation of the semi-cylindrical shell center is increased by hydrostatic pressure. The adopted ALE method amalgamates the benefits of the Lagrangian and Eulerian methods. The Lagrange method is primarily applicable to solid materials. Its significant limitation lies in its inability to handle large deformations. The Euler method is generally more suitable for describing the behavior of fluids and gases, but the interface tracking of different materials is computationally large and not ideal. Due to its unique nodal motion, the Arbitrary Lagrangian–Eulerian (ALE) method amalgamates the benefits of both the Lagrangian and Eulerian methods [5]. However, the study considered the effect of explosion shock waves, but it did not consider the impact of bubble pulsation. In future research, we will consider performing relevant research, further determining the effect of bubble pulsation. In addition, with the increasing number of intentional or unintentional underwater explosions, enhancing the protection performance of underwater bottom-sitting shell structures is crucial. Also, indoor and outdoor underwater explosion

model tests should be conducted to enrich and develop research on underwater explosions in bottom-sitting shell fields.

6. Conclusions

This paper uses finite element numerical simulation to investigate the damage characteristics and dynamic response of bottom-sitting shell structures under underwater shock waves. The effects of the shock wave transmission medium, explosive equivalent, explosive distance, hydrostatic pressure, and reinforcement on the damage characteristics and dynamic response of semi-spherical and semi-cylindrical bottom-sitting RC shell structures were studied using validated numerical models. The main conclusions are as follows:

- (1) The damage and vertical center deformation of semi-spherical and semi-cylindrical RC shells under underwater shock waves are significantly greater than those under air shock waves.
- (2) The damage to the semi-spherical RC shell is mainly concentrated in the lower part and the center of the semi-spherical RC shell, and gradually extends from the lower part to the center of the semi-spherical RC shell with an increase in explosive equivalent. The damage to the semi-cylindrical RC shell is mainly concentrated in the junction of the semi-cylindrical RC shell and side walls at both ends, the constraint position of the semi-cylindrical RC shell, and the center of the semi-cylindrical shell. The damaged area gradually extends from the junction between the semi-cylindrical RC shell and side walls at both ends, and the restraint on both sides of the semi-cylindrical shell to the center of the semi-cylindrical shell with an increase in explosive equivalent.
- (3) The damage and vertical center deformation of the semi-spherical and semi-cylindrical RC shells show a gradually increasing trend with an increase in explosive equivalent or decrease in explosive distance. Meanwhile, the damage to the inner surface of the semi-spherical RC shell is more severe than the outer surface.
- (4) The overall damage and vertical center deformation of the semi-spherical and semi-cylindrical RC shell can be reduced by the bottom reinforcement and an increase in the diameter of the steel bar within the diameter range of 10–16 mm. However, the effect of the diameter of the steel bar on the vertical center displacement of the semi-cylindrical RC shell is lower than for the semi-spherical RC shell.
- (5) The ‘hoop effect’ caused by hydrostatic pressure restrains the horizontal convex deformation and slightly decreases the macroscopic damage and vertical center deformation of the semi-spherical RC shell with an increase in hydrostatic pressure within the range of 0–2.0092 MPa. The hydrostatic pressure restrains the horizontal convex deformation of the semi-cylindrical RC shell. However, the inward concave deformation of the semi-cylindrical shell center is increased by hydrostatic pressure, inducing an increase in the damage and center vertical deformation of the semi-cylindrical RC shell.

Author Contributions: Conceptualization, F.L. and X.Z.; methodology, F.L. and L.X.; software, F.L. and J.Z.; validation, F.L., X.Z. and L.X.; formal analysis, F.L., J.Z. and Z.L.; investigation, F.L., Z.L. and L.T.; resources, J.Z. and L.X.; data curation, F.L. and X.Z.; writing—original draft preparation, F.L., Z.L., J.W. and L.T.; writing—review and editing, F.L., Z.L. and J.W.; visualization, F.L. and L.T.; supervision, F.L.; project administration, F.L. and X.Z. All authors have read and agreed to the published version of the manuscript.

Funding: This research received no external funding.

Institutional Review Board Statement: Not applicable.

Informed Consent Statement: Not applicable.

Data Availability Statement: The data used to support the findings of this study are available from the corresponding author upon request. The data are not publicly available due to privacy.

Acknowledgments: We would like to express our sincerest gratitude to the anonymous unidentified reviewers for providing us with constructive and insightful comments and suggestions.

Conflicts of Interest: The authors declare no conflicts of interest.

References

1. Avachat, S.; Zhou, M. Response of submerged metallic sandwich structures to underwater impulsive loads. *J. Mech. Mater. Struct.* **2015**, *10*, 17–41. [[CrossRef](#)]
2. Yang, G.D.; Fan, Y.; Wang, G.H.; Gao, Q.D.; Deng, K.; Wang, F. Numerical study on dynamic response of submerged tunnel subjected to underwater explosion. *Soil Dyn. Earthq. Eng.* **2022**, *156*, 107216. [[CrossRef](#)]
3. Yang, G.D.; Wang, G.H.; Fan, Y.; Wang, F.; Lu, W.B.; Zhao, J.S. Dynamic response and performance of submarine tunnel subjected to surface explosions. *Mar. Struct.* **2021**, *80*, 103091. [[CrossRef](#)]
4. Yang, G.D.; Wang, G.H.; Lu, W.B.; Yan, P.; Chen, M. Damage assessment and mitigation measures of underwater tunnel subjected to blast loads. *Tunn. Undergr. Space Technol.* **2019**, *94*, 103131. [[CrossRef](#)]
5. Mussa, M.H.; Mutalib, A.A.; Hamid, R.; Naidu, S.R.; Radzi, N.A.M.; Abedini, M. Assessment of damage to an underground box tunnel by a surface explosion. *Tunn. Undergr. Space Technol.* **2017**, *66*, 64–76. [[CrossRef](#)]
6. Wang, Y.G.; Liao, C.C.; Wang, J.H.; Jeng, D.S. Dynamic response of pipelines with various burial depth due to underwater explosion. *Ocean Eng.* **2018**, *164*, 114–126. [[CrossRef](#)]
7. Kristoffersen, M.; Minoretti, A.; Børvik, T. On the internal blast loading of submerged floating tunnels in concrete with circular and rectangular cross-sections. *Eng. Fail. Anal.* **2019**, *103*, 462–480. [[CrossRef](#)]
8. Luo, G.; Zhang, Y.L.; Ren, Y.; Guo, Z.R.; Pan, S.K. Dynamic response analysis of submerged floating tunnel subjected to underwater explosion-vehicle coupled action. *Ocean Eng.* **2021**, *232*, 109103. [[CrossRef](#)]
9. Nie, B.C.; Zhang, H.Q. Hoop and axial plastic buckling modes of submerged cylindrical shells subjected to side-on underwater explosion shock wave. *Mar. Struct.* **2022**, *84*, 103200. [[CrossRef](#)]
10. Brochard, K.; Sourne, H.L.; Barras, G. Extension of the string-on-foundation method to study the shock wave response of an immersed cylinder. *Int. J. Impact Eng.* **2018**, *117*, 138–152. [[CrossRef](#)]
11. Huang, H. Scattering of Spherical Pressure Pulses by a Hard Cylinder. *J. Acoust. Soc. Am.* **1975**, *58*, 310–317. [[CrossRef](#)]
12. Jin, Q.K.; Ding, G.Y. A finite element analysis of ship sections subjected to underwater explosion. *Int. J. Impact Eng.* **2011**, *38*, 558e566. [[CrossRef](#)]
13. Hung, C.F.; Lin, B.J.; Hwang-Fuu, J.J.; Hsu, P.Y. Dynamic response of cylindrical shell structures subjected to underwater explosion. *Ocean Eng.* **2009**, *36*, 564–577. [[CrossRef](#)]
14. Peng, Y.X.; Zhang, A.M.; Ming, F.R. Numerical simulation of structural damage subjected to the near-field underwater explosion based on SPH and RKPM. *Ocean Eng.* **2021**, *222*, 108576. [[CrossRef](#)]
15. Nayak, S.; Lyngdoh, G.A.; Shukla, A.; Das, D.S. Predicting the near field underwater explosion response of coated composite cylinders using multiscale simulations, experiments, and machine learning. *Compos. Struct.* **2022**, *283*, 115157. [[CrossRef](#)]
16. Long, N.V.; Thinh, T.I.; Bich, D.H.; Tu, T.M. Nonlinear dynamic responses of sandwich-FGM doubly curved shallow shells subjected to underwater explosions using first-order shear deformation theory. *Ocean Eng.* **2022**, *260*, 111886. [[CrossRef](#)]
17. Zhao, Z.W.; Zhou, S.; Gao, H.; Liu, H.Q. Predictions of compression capacity of randomly corroded spherical shells based on artificial neural network. *Ocean Eng.* **2022**, *257*, 111668. [[CrossRef](#)]
18. Guo, J.; Jiang, S.P.; Zhang, Z.Y. Fire Thermal Stress and Its Damage to Subsea Immersed Tunnel. In Proceedings of the 2nd International Symposium on Submerged Floating Tunnels and Underwater Tunnel Structures, Chongqing, China, 16–18 December 2016.
19. MacKay, J.R.; Jiang, L.; Glas, A.H. Accuracy of nonlinear finite element collapse predictions for submarine pressure hulls with and without artificial corrosion damage. *Mar. Struct.* **2011**, *24*, 292–317. [[CrossRef](#)]
20. Zhang, J.; Lin, Z.K.; Wang, F.; Zhao, T.; Zhu, Y.M. Ultimate strength of externally pressurised steel spheres containing through-thickness defects. *Int. J. Press. Vessel. Pip.* **2022**, *199*, 10470. [[CrossRef](#)]
21. Zhang, J.; Zhang, M.; Tang, W.X.; Wang, W.B.; Wang, M.L. Buckling of spherical shells subjected to external pressure: A comparison of experimental and theoretical data. *Thin-Walled Struct.* **2017**, *111*, 58–64. [[CrossRef](#)]
22. Ismail, M.S.; Mahmud, J.; Jailani, A. Buckling of an imperfect spherical shell subjected to external pressure. *Ocean Eng.* **2023**, *275*, 114118. [[CrossRef](#)]
23. Lu, C.F.; Chen, W.Q.; Shao, J.W. Semi-analytical three-dimensional elasticity solutions for generally laminated composite plates. *Eur. J. Mech. A-Solid* **2008**, *27*, 899–917. [[CrossRef](#)]
24. Wang, H.M. Dynamic electromechanical behavior of a triple-layer piezoelectric composite cylinder with imperfect interfaces. *Appl. Math. Model* **2011**, *35*, 1765–1781. [[CrossRef](#)]
25. Yang, G.D.; Fan, Y.; Wang, G.H.; Cui, X.Z.; Leng, Z.D.; Lu, W.B. Blast resistance of air-backed RC slab against underwater contact explosion. *Def. Technol.* **2023**, *28*, 236–250. [[CrossRef](#)]
26. Liu, Z.Y.; Zhou, X.X.; Xiao, L.; Li, X.; Lin, F.T. Dynamic response and damage characteristics of special blast-resistant door structure subjected to underwater explosion. *Structures* **2023**, *57*, 105262. [[CrossRef](#)]

27. Xie, L.X.; Lu, W.B.; Zhang, Q.B.; Jiang, Q.H.; Chen, M.; Zhao, J. Analysis of damage mechanisms and optimization of cut blasting design under high in-situ stresses. *Tunn. Undergr. Space Technol.* **2017**, *66*, 19–33. [[CrossRef](#)]
28. Riedel, W.; Thoma, K.; Hiermaier, S.; Schmolinske, E. Penetration of Reinforced Concrete by BETA-B-500 Numerical Analysis using a New Macroscopic Concrete Model for Hydrocodes. In Proceedings of the 9th International Symposium on the Effects of Munitions with Structures, Berlin-Strausberg, Germany, 3–7 May 1999.
29. Zhou, Q.; Qi, L. Analysis and comparison of 5 different common anti-explosion concrete material models of LS-DYNA software. *Concrete* **2019**, *11*, 43–49. (In Chinese) [[CrossRef](#)]

Disclaimer/Publisher’s Note: The statements, opinions and data contained in all publications are solely those of the individual author(s) and contributor(s) and not of MDPI and/or the editor(s). MDPI and/or the editor(s) disclaim responsibility for any injury to people or property resulting from any ideas, methods, instructions or products referred to in the content.